MINISTÈRE DE L'ENSEIGNEMENT SUPÉRIEUR ET DE LA RECHERCHE SCIENTIFIQUE

UNITÉ DE FORMATION ET DE RECHERCHE - SCIENCES DES STRUCTURES DE LA MATIÈRE ET DE TECHNOLOGIE

REPUBLIQUE DE CÔTE D'IVOIRE
UNION-DISCIPLINE-TRAVAIL

**Félix Houphouët Boigny University**

N°: 838

# MASTER IN ENERGY AND GREEN HYDROGEN

SPECIALITY: Green Hydrogen Production and Technology

## MASTER THESIS:

Subject/Topic:

**ELECTROCHEMICHAL CHARACTERIZATION OF SYMMETRICAL PRASEODYMIUM DOPED CERIA ELECTRODES FOR SOLID OXIDE CELLS**

Presented on the 26th September 2025 and by:

**Jean-Baptiste AHOUANDJINOU**

**Jury**

| | |
|---|---|
| Dr (MC) ZAHIRI Eric Pascal | **President** |
| Dr(MC) ESSY Kouadio Fodjo | **Examiner** |
| Dr. FOFANA Daouda | **Major Supervisor** |
| Prof. Rüdiger-A.Eichel | **Co-Supervisors** |
| Rishabh Kumar | |

**Academic year: 2024-2025**

## FOREWORD AND ACKNOWLEDGMENT

I would like to acknowledge and express my sincere gratitude to the following individuals and organizations who have played a significant role in shaping my educational journey and academic success.

Thanks to BMFTR and WASCAL in awarding me this scholarship that made my academic journey possible.

I extend my thanks to the president of the University Félix Houphouët Boigny Prof. Ballo Zie, to the president of the university of Lome Prof. Adama Mawulé Kpodar, and to the president of the University Abdoul Moumouni Prof. Baragé MOUSSA. I am grateful to the vice chancellor of Forschungszentrum Jülich and the director of the institute IET-1, Prof. Dr. Rüdiger-A. Eichel for his constant encouragement, expertise, and guidance during my studies., where I completed my internship. My thanks to the team members of Wascal Côte d'Ivoire.

I extend my thanks to my Major-Supervisor, Dr Daouda FOFANA, for his valuable insights and contributions that have enhanced the quality of my academic work. I would like to acknowledge the jury president, Dr (MC) ZAHIRI Eric Pascal, and the jury examiner, Dr (MC) ESSY Kouadio Fodjo, for their valuable time, expertise, and evaluation of my academic achievements.

Thank you to the team members from Togo and Niger who were involved in the first and second semesters of my academic journey, for their collaboration and support. I am particularly grateful to my parents, Toussaint AHOUANDJINOU and Elise HOUEWASSOUDE, and my brothers, Giovania, Fadelle, and Parfait AHOUANDJINOU, who have been nothing but supportive and caring throughout my entire life. I feel lucky to be surrounded by such a loving family.

I cannot end these acknowledgments without mentioning the head of the Fundamental Electrochemistry Department, Dr Till. Frömling, Dr Vaibhav. Vibhu and my daily supervisor, Rishabh. KUMAR for their unwavering support, expert advice, and encouragement throughout this internship. My heartfelt gratitude for their exceptional leadership and guidance as my supervisors, and for the work atmosphere that they created during my stay. Thank you to all the team members of IET-1.

**ABSTRACT**

Decarbonizing industry at scale requires robust high-temperature electrolysers whose fuel electrodes avoid the long-term degradation modes of nickel-based cermets. This thesis evaluates symmetrical praseodymium-doped ceria (PDC) as a nickel-free mixed ionic–electronic conductor (MIEC) fuel electrode for solid oxide cells. Symmetrical Au/PDC10/GDC/8YSZ/GDC/PDC10 (gold/praseodymium-doped ceria 10%/gadolinium doped ceria/8% yttrium stabilized zirconia/gadolinium doped/praseodymium-doped ceria 10%/gold) ceria cells with two PDC thicknesses (~46 µm and ~19 µm) were prepared; their microstructure was examined by scanning electron microscopy (SEM) and electrochemical behavior probed by impedance spectroscopy under controlled $H_2/H_2O$ mixtures and 750 – 900 °C conditions. Impedance spectra were decomposed using distribution-of-relaxation-times (DRT) analysis and equivalent-circuit modeling (ECM); Arrhenius and gas-partial-pressure studies yielded apparent activation energies and reaction orders. The thinner (~19 µm) electrode exhibited lower ohmic and polarization resistances and was selected for detailed analysis. Three reproducible processes were resolved:

- a dominant low-frequency, $H_2$-sensitive process consistent with hydrogen adsorption/dissociation.
- a high-activation-energy, gas-insensitive process assigned to intrinsic electrode charge transfer;
- and a low-activation-energy Gerischer-like contribution of unclear origin.

From these assignments, a hydrogen-controlled surface charge-transfer is identified as the rate-determining step under the studied conditions. By delivering well-defined quantitative kinetics and a correlation between relaxation times and physical steps, this work positions PDC10 as a promising Ni-free fuel electrode, along with providing guiding principles for improving activity and stability in the design of future electrodes.

**Keywords:** Praseodymium-doped ceria; solid oxide cells; electrochemical impedance spectroscopy; distribution of relaxation times; nickel-free electrode.

**RESUME**

La décarbonation industrielle à grande échelle nécessite des électrolyseurs à haute température robustes dont les électrodes à combustible évitent les modes de dégradation à long terme des cermets à base de nickel. Cette thèse évalue la cérine symétrique dopée au praséodyme (PDC) comme électrode à combustible sans nickel, de type conducteur mixte ionique–électronique (MIEC), pour des cellules à oxyde solide. Des cellules symétriques Au/PDC10/GDC/8YSZ/GDC/PDC10 (or/céria dopée au praséodyme 10%/céria dopée au gadolinium/8% zircone stabilisée à l'yttrium/dopée au gadolinium/céria dopée au praséodyme 10%/or) avec deux épaisseurs de PDC (46 µm et 19 µm) ont été soigneusement préparées ; leur microstructure a été analysée par microscopie électronique à balayage (SEM) et le comportement électrochimique a été examiné par spectroscopie d'impédance dans des mélanges contrôlés $H_2/H_2O$ et à des températures variant de 750 à 900 °C. Les spectres d'impédance ont été traités via l'analyse des temps de relaxation (DRT) et de la modélisation par circuit équivalent (ECM) ; les études d'Arrhenius et de pression partielle des gaz ont mis en évidence des énergies d'activation apparentes et des ordres de réaction. L'électrode la plus fine (~19 µm) a montré des résistances ohmiques et de polarisation inférieure, ce qui a conduit à sa sélection pour une étude plus détaillée. Trois processus reproductibles ont été résolus :

- un processus dominant à basse fréquence, sensible à $H_2$, compatible avec l'adsorption/dissociation de l'hydrogène ;
- un processus à haute énergie d'activation, insensible à la composition gazeuse, attribué au transfert de charge intrinsèque de l'électrode ;
- et une contribution de type Gerischer à faible énergie d'activation d'origine incertaine.

A partir de ces analyses, un transfert de charge de surface contrôlé par l'hydrogène est identifié comme l'étape déterminante de la réaction dans les conditions étudiées. En fournissant une cinétique quantitative bien définie et une corrélation entre les temps de relaxation et les étapes physiques, ce travail positionne le PDC10 comme une électrode combustible prometteuse sans nickel, tout en apportant des principes directeurs pour améliorer l'activité et la stabilité dans la conception des électrodes futures.

**Mots clés :** oxyde de cérium dopé au praséodyme ; cellules à oxyde solide ; spectroscopie d'impédance électrochimique ; distribution des temps de relaxation ; électrode sans nickel.

## ACRONYMS AND ABREVIATIONS

**ASR:** Area specific resistance

**CO:** Carbon monoxide

**$CO_2$:** Carbon dioxide

**CPE:** Constant phase element

**CNLS:** Complex-nonlinear-least-squares

**$C_eO_2$:** Cerium oxide

**DRT:** Distribution of relaxation times

**$E_a$:** Activation energy ($kJ.mol^{-1}$)

**EIS:** Electrochemical impedance spectroscopy

**ECM:** Equivalent circuit model

**f:** Frequency (Hz)

**GDC:** Gadolinium-doped ceria

**$H_2$:** Hydrogen

**$H_2O$:** Water (steam)

**LSM:** Strontium-doped lanthanum manganite

**LSCF:** Lanthanum-strontium cobalt ferrite

**LSC:** Lanthanum strontium cobaltite

**MIEC:** Mixed ionic-electronic conductor

**Ni:** Nickel

**$N_2$:** Nitrogen

**OCV:** Open circuit voltage

**$O_2$:** Oxygen

**PDC:** Praseodymium-doped ceria

**$R_\Omega$:** Ohmic resistance

**$R_p$:** Polarization resistance

**SEM:** Scanning electron microscopy

**SOC:** Solid oxide cell

**SOEC:** Solid oxide electrolysis cell

**SOFC:** Solid oxide fuel cell

**TEC:** Thermal expansion coefficient

**TBP:** Triple-phase boundary

**T:** Temperature (K)

**Z:** Impedance (Ω)

**8YSZ:** 8% yttrium stabilized zirconia

**LIST OF FIGURES**

**TABLE OF CONTENTS**

# GENERAL INTRODUCTION

## GENERAL INTRODUCTION

Fossil fuels have powered modern energy systems for decades, but their combustion emits significant amounts of carbon dioxide and other greenhouse gases, which increase atmospheric concentrations and contribute to global warming. Because of the climate, economic, and policy pressures to decarbonize, the global energy system is now transitioning from a fossil-fuel-based model toward one increasingly supplied by renewable electricity [1]. Rapid improvements in the cost-performance of renewable technologies have enabled this shift. However, replacing fossil fuels entirely is challenging because of the intermittency of solar and wind energy. To keep supply and demand balanced, a surplus of renewable electricity must be stored or converted into other energy carriers for later use.

Electrochemical conversion is a promising route for that: electrolysers transform surplus electricity into chemical energy ($H_2$ or CO). Electrolysers are commonly grouped by operating temperature into low-temperature devices (Alkaline, Proton exchange membrane PEM, anion exchange membrane AEM) and high-temperature solid oxide electrolysis cells (SOECs) [2], [3], [4]. Low-temperature electrolysers operate at modest temperatures and can be built from relatively inexpensive materials such as nickel-based materials for the catalyst, stainless steel for electrodes, and Alkaline electrolyte like NaOH. However PEM systems typically require costly catalysts, and they all face challenges with impurity tolerance and water management [5], [6], [7]. SOECs operate at elevated temperatures, where thermodynamics and kinetics for $H_2O/CO_2$ splitting/reduction are more favorable. They can co-electrolyze $CO_2$ and $H_2O$ and even operate reversibly as fuel cells (rSOCs), and they offer broader fuel flexibility (hydrocarbons, syngas) [8], [9]. At the same time, SOECs suffer from durability and degradation challenges related to high operating temperatures and complex electrode/electrolyte interaction [10].

A central materials challenge for SOECs is the fuel electrode. The conventional Ni-YSZ cermet anode combines excellent electronic conductivity and catalytic activity, but it is prone to degradation mechanisms (Ni agglomeration, carbon deposition, sulfur poisoning, redox-driven volume changes) that reduce active area and long-term performance under realistic feeds and thermal cycles [11], [12], [13]. Mixed ionic-electronic conductors (MIECs) such as doped ceria and certain perovskites have therefore attracted attention as Ni-free alternatives: by providing ionic and electronic transport, they extend the reactive region beyond a narrow triple-phase boundary (TPB) into a broader active interface (sometimes called a double-phase or distributed

active region), which can increase the electrochemically available area and simplify electrode architectures [14], [15]. Nevertheless, ceria-based electrodes bring trade-offs: while doping improves oxide-ion conductivity, electronic conductivity can remain limited, and heavy dopants (notably Pr at high concentration) can cause chemical expansion and stability problems. Ni addition to ceria (Ni-GDC) mitigates some limitations (such as chemical instability in reducing atmosphere, sintering, and microstructural degradation), but reintroduces Ni-related degradation modes (migration, aggregation), so the search for robust Ni-free doped-ceria electrodes is an active and practically important research direction [15].

Symmetrical single-chamber cells are an effective diagnostic tool to investigate electrode kinetics in a controlled and unambiguous way. In a symmetrical cell the same electrode material is applied to both sides of the electrolytes, and in a single-chamber configuration, both electrodes are exposed to the same controlled gas atmosphere during measurements. This yields a measured impedance spectrum composed of two equal electrode contributions plus the electrolyte term, which makes electrochemical impedance spectroscopy analyzing far more reliable.

Considering this background, the present work focuses on the electrochemical characterization of symmetrical praseodymium-doped ceria (PDC) electrodes for solid oxide cells. Pr-doping introduces mixed-valence behavior ($Pr^{3+}/Pr^{4+}$) which can enhance electronic conductivity while preserving oxide-ion transport. However, it is imperative to note that excessive Pr content can result in chemical expansion [16]. We therefore studied the sandwich composition of $Pr_{0.1}Ce_{0.9}O_{2-\delta}$ (PDC10) integrated in cell configuration with a GDC ($Ce_{0.8}Gd_{0.2}O_{0.1}$) barrier layer and an 8 mol% $(ZrO_2)_{0.92}(Y_2O_3)_{0.08}$ electrolyte.

The work aims to investigate the possible physicochemical processes that appear on PDC10 electrodes in the $H_2/H_2O$ system over a temperature range from 750 °C to 900 °C, and to compare the outcomes with literature.

This thesis will address the following specific points:

- What physicochemical processes occur at the PDC electrodes?
- Which process is the rate-determining step for $H_2$ production?
- How do electrode thickness, temperature, and gas composition influence the ohmic and polarization resistances?

In the following chapter, an overview of solid oxide cells is presented, along with an exposition of their operating principles, and the role of Pr-doped ceria as an electrode material with an emphasis on the microstructure of the electrode, degradation issues, and the methodology employed for electrochemical analysis. The experimental procedures, including cell fabrication, characterization techniques, and electrochemical testing, are described in Chapter 2. Chapter 3 presents the primary results, with a particular emphasis on impedance spectra, DRT/ECM analysis, and the impact of gas composition on electrode processes, followed by a discussion of the identified rate-determining steps.

# CHAPTER 1: LITERATURE REVIEW

# Chapter 1: LITERATURE REVIEW

## Introduction

Solid oxide cells (SOCs) first emerged in the 1980s, especially for NASA space exploration. They were motivated by recycling carbon dioxide and water into fuel and oxygen. SOCs have recently been the focus of studies from the nanoscale to the macroscale and from the electrode to the stack level [17].

The present chapter is an examination of the fundamentals of SOC operation, with a comparative analysis of symmetrical and asymmetrical cell designs. It further emphasizes the importance of a symmetrical cell in the evaluation of physical and chemical processes that may be occurring within the electrochemical system. Furthermore, it elucidates the underlying principle of symmetry in the interpretation of impedance spectra.

## 1.1. Solid Oxide Cells

SOCs are high-temperature, reversible electrochemical devices. They can operate either as Solid Oxide Fuel Cells (SOFCs), generating electrical energy from fuel like Hydrogen or methane, or as Solid Oxide Electrolysis Cells (SOECs), using electrical energy to split water into hydrogen or carbon dioxide into carbon monoxide. Figure 1 illustrates the different components of SOEC: the anode (air electrode, where oxidation occurs), the cathode (fuel electrode, where reduction occurs), and electrolytes. The electrolytes act as insulators for electrons while facilitating ion conduction, allowing electrons involved in electrochemical reactions at the electrode to move through the external circuit [18].

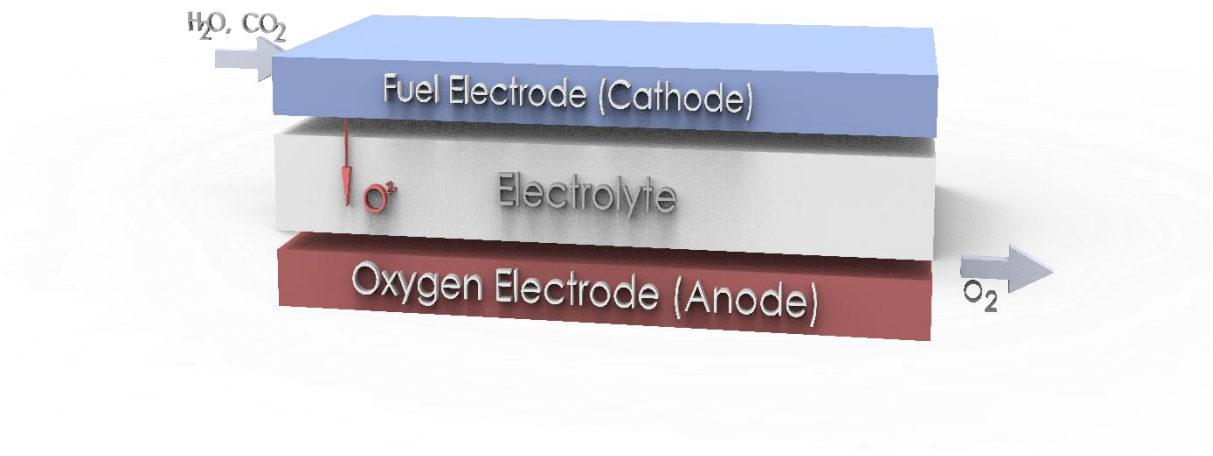


Figure 1: SolidWorks model of the SOEC single cell

The high operating temperatures of SOCs are not arbitrary, but stem directly from the material and transport requirements of the cell.

### 1.1.1. Why do SOCs operate at high temperatures?

SOCs generally operate at high temperatures within a range of 600 °C to 1000 °C. This is due to three key factors:

#### 1.1.1.1. Faster reaction kinetics

High temperatures accelerate surface reactions (water dissociation, $O^{2-}$ transport, electron transfer), significantly improving cell efficiency. The kinetics of the possible reactions that may be occurring in the given electrochemical system are facilitated by certain phenomena, such as the breaking and making of reactant and product bonds, and surface diffusion.

#### 1.1.1.2. Ionic conductivity

State-of-the-art oxygen-ion-conducting electrolytes such as yttria-stabilized zirconia (YSZ) and scandia-doped zirconia (SDZ) only conduct $O^{2-}$ ions efficiently at high temperatures. Although YSZ has become a prevalent electrolyte material owing to its noteworthy chemical and mechanical stability, its low ionic conductivity at intermediate temperatures limits its practicality[19], [20]. Gadolinium-Doped Ceria (GDC) has gained popularity as an alternative to YSZ; however, ceria-based materials demonstrate electronic leakage under low oxygen partial pressures, making them unsuitable as electrolytes under such conditions [21].

Additionally, several criteria are crucial for the selection of a suitable electrolyte materials for SOCs [18]:

- It must exhibit thermal, chemical, and structural stability in the cell operation range.
- It must be dense to prevent crossover of gases.
- It must demonstrate high ionic conductivity (exceeding $10^{-2}$S/cm), which is a prerequisite when considering its ability to concurrently exhibit insulating behavior to electronic conduction.
- Given the electrolyte's position between the fuel and oxygen electrodes, it is important that its thermal expansion coefficient matches well with that of the proximate electrodes. This congruence is pivotal in ensuring uniformity at the electrode-electrolyte interface, thereby facilitating efficient ion transport across the interface.

### 1.1.1.3. Thermodynamics advantage

The thermodynamic advantage of elevated operating temperatures is evident in the reduced electrical energy demand required for the dissociation of water and carbon dioxide. This can be quantified using the Gibbs free energy equation. The energy demand for the electrolysis reaction is determined by the process enthalpy change (ΔH), which comprises the entropy term (TΔS) as thermal energy (ΔQ) and the Gibbs free energy change (ΔG) as electrical energy, which is the available energy to do useful work. The following expression demonstrates the relationship among the thermodynamic magnitudes [22]:

$$\Delta \boldsymbol{H} = \Delta \boldsymbol{G} + \boldsymbol{T}\Delta \boldsymbol{S} \quad (1)$$

ΔH is the enthalpy change, T is the temperature, and ΔS is the entropy change.

Concurrently, as the temperature rises, there is a decline in the electrical energy, ΔG, whereas the heat requirement increases (Figure 2).

The electrochemical reaction, also known as electrolysis, is characterized as endothermic (ΔH >0) and nonspontaneous (ΔG >0). As illustrated in Figure 2, the relationship between energy demand and the requisite cell voltage at 0.1 MPa steam pressure is demonstrated. This clearly shows a decline in the demand for electrical energy (ΔG) and an increase in heat energy demand (ΔQ) with increasing temperature. This trade-off is financially advantageous because the cost of electrolytic hydrogen is predominantly attributed to the consumption of electricity, accounting for over two-thirds of its total expenses. Despite a modest increase in total energy demand, a more pronounced decline in the electrical energy demand is evident. If the increase in heat energy demand is met by an external heat source, or waste heat from high-temperature industrial processes, the cost of hydrogen production could be reduced by operating at higher temperatures [23].

The minimum cell voltage, otherwise referred to as the reversible cell voltage, $V_r$, required for the electrolysis reaction to occur, is expressed as Gibbs' free energy change, or ΔG, from a thermodynamic perspective, as outlined below [22]:

$$\boldsymbol{V_r} = \frac{-\Delta \boldsymbol{G}}{\boldsymbol{n} * \boldsymbol{F}} \quad (2)$$

where n is the number of electrons per mole of product and F is the Faraday constant.

In other words, the Nernst equation quantifies the shifts in the reversible voltage required for electrolysis that result from changes in temperature and gas composition.

The minimum voltage required for electrolysis when heat energy TΔS is supplied by electricity is known as the thermoneutral voltage ($V_{tn}$). This is the predominant condition in most commercial electrolysis systems.

$$V_{tn} = \frac{\Delta H}{n * F} \tag{3}$$

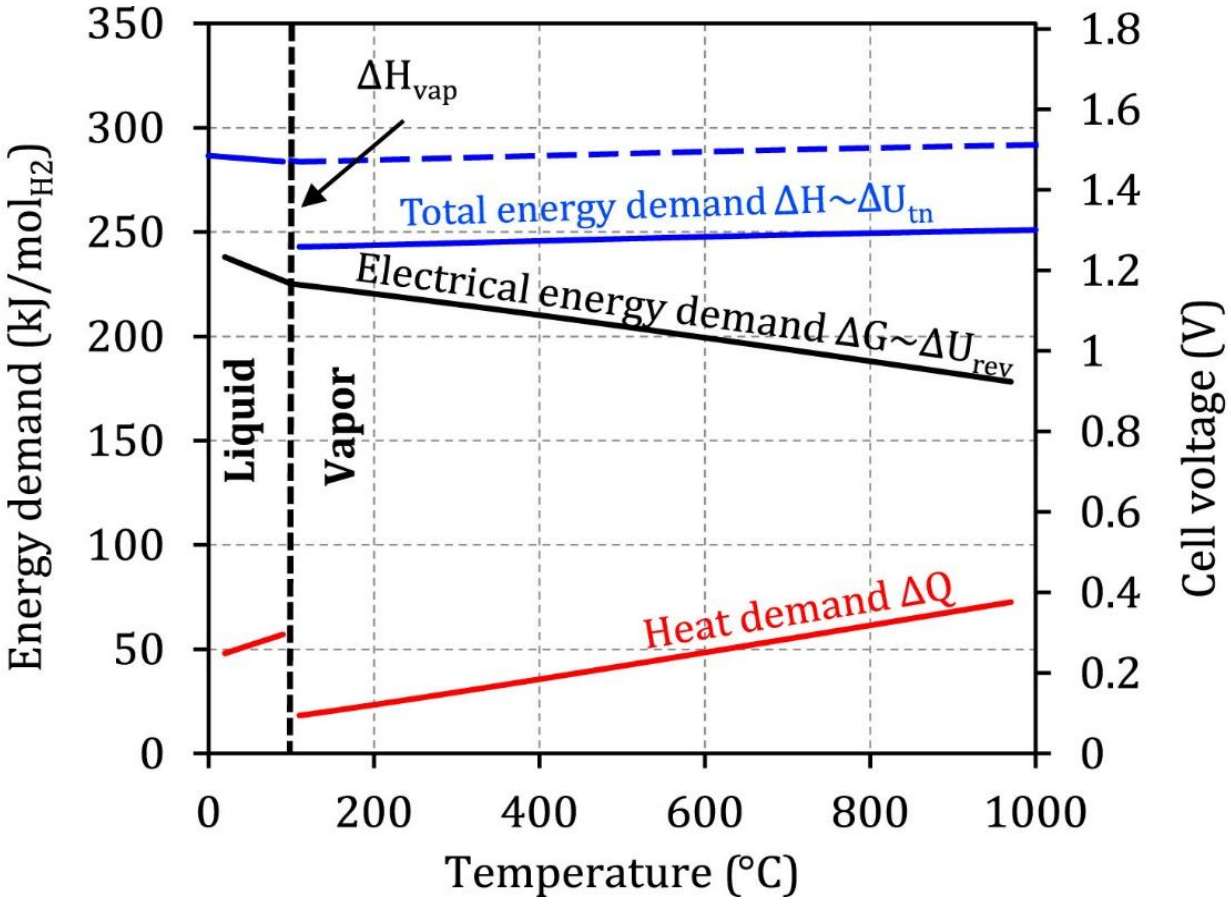


Figure 2: Total (ΔH), thermal (Q), and electrical (ΔG) energy demands of an ideal electrolysis process as a function of temperature. Adapted from [24].

### 1.1.2. SOFC vs SOEC reversible operation

The governing principles of electrochemistry that enable electrolysis cells to efficiently synthesize fuels (hydrogen and carbon monoxide) or oxygen can also be applied in reverse to operate them as a fuel cell for electricity generation. Electrolysis involves splitting gaseous species such as water vapor ($H_2O$), or carbon dioxide ($CO_2$), into their constituent molecules ($H_2$, CO, $O_2$) through the application of an external voltage. Conversely, in fuel cell mode, chemical energy stored in fuels ($H_2$, CO) is converted directly into electricity via oxidation with oxygen [25].

Figure 3 shows a schematic representation of an SOFC and SOEC cell in the $H_2O/H_2$ system. During electrolysis, the application of a sufficiently high electrical potential difference across the cell results in the movement of oxygen ions $O^{2-}$ from the cathode to the anode through the electrolyte [26]. In SOFC mode, the process is reversed: oxygen ions migrate from the oxygen electrodes to the fuel electrodes, where they react with hydrogen to produce water and electrons.

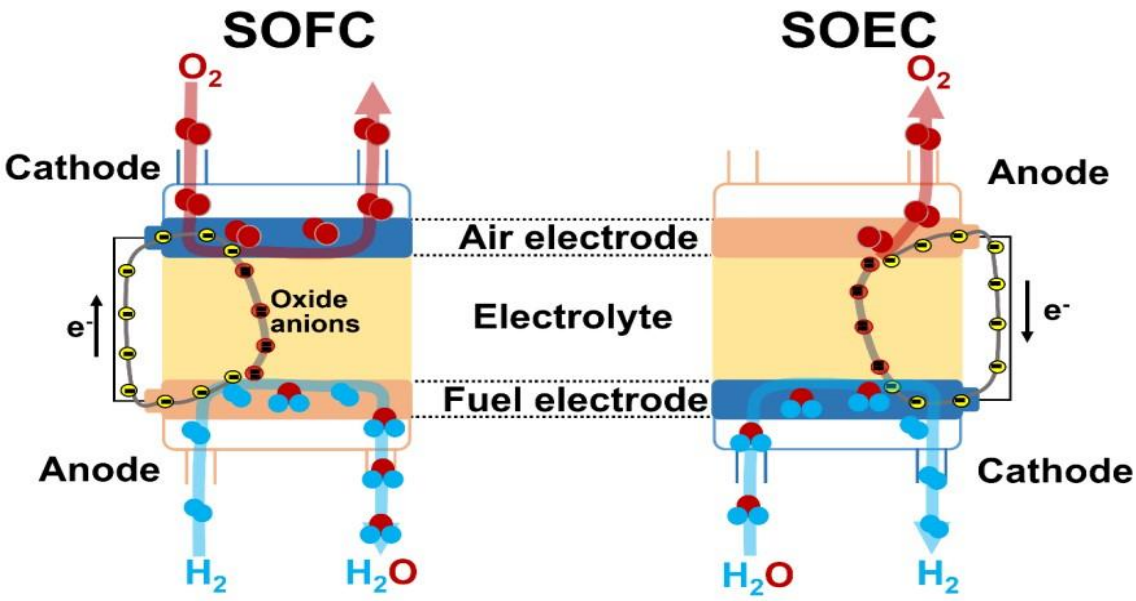


Figure 3: A schematic representation of the reversibility of an SOFC (left) and SOEC (right) for H2O/H2 operation [26].

The reduction/oxidation (red/ox) reaction can be subdivided into two half-reactions [27]. At the cathode, water molecules combine with electrons from the external circuit and undergo dissociation, resulting in the formation of hydrogen and oxygen ions (Equation 4). At the anode, the production of oxygen gas ($O_2$) is described by equation 5. The produced oxygen gas can be collected at the anode side, while the other desired gases, such as hydrogen ($H_2$) can be collected at the cathode side [27].

$$\boldsymbol{H_2O + 2e^- \rightleftarrows O^{2-} + H_2} \tag{4}$$

$$\boldsymbol{O^{2-} \rightleftarrows \frac{1}{2}O_2 + 2e^-} \tag{5}$$

The electrode at which reaction (4) occurs remains constant and is designated as the cathode in the electrolysis cells, where the reaction progresses from left to right. In SOFC mode, the reaction progresses from right to left, thus identifying the anode as the electrode of interest. To avoid any potential ambiguity, the electrode on which reaction (4) occurs is always referred to

as the fuel electrode, whereas the electrode hosting reaction (5) is denoted as the oxygen electrode [28].

It is imperative to acknowledge the shift in the sign of the overall reaction enthalpy during the operation of both SOFC and SOEC. Under standard conditions $\Delta H^{o}_{H_2/O_2} = -241.8\,kJ/mol$, so that SOFCs are exothermic (heat-releasing). Driving these same reactions in reverse (SOEC mode) flips the sign, and ΔH becomes +241.8 kJ/mol, making the process endothermic [29]. This is exactly the enthalpy term that appears in the thermoneutral voltage, $V_{tn}$, discussed in section 1.1.1.3.

### 1.1.2. Cell architecture

#### 1.1.2.1. Asymmetrical cell

The development of SOCs, particularly advancements in material and structural design, has provided critical insights for optimization. Traditional SOCs have a "sandwich" architecture with a dense electrolyte positioned between two porous cathode and anode layers on opposing sides. Generally, the anode and cathode are composed of different materials. For instance, the most conventional $Ni - Y_{0.08}Zr_{0.92}O_{2-\delta}(YSZ)/YSZ/La_{0.8}Sr_{0.2}MnO_{3-\delta}(LSM)$ cell configuration can be characterized as an A/B/C structure, which is an asymmetrical configuration with different materials designated as traditional SOCs [30].

The preparation of asymmetrical cells necessitates a series of energy-intensive steps [31]:

- The electrolyte support prepared through the processes of tape-casting or dry pressing
- The process of screen-printing is employed for the purpose of depositing the anode and cathode layers
- The electrolytes and electrodes are subjected to a sequence of high-temperature sintering (>1300°C) processes

Furthermore, asymmetric cells are subject to the following limitations (Figure 4):

- High fabrication cost due to material diversity and multi-step sintering
- Dual electrode-electrolyte interfaces, which demand precise chemical compatibility and raise delamination risks during thermal cycling
- The thermal expansion coefficient (TEC) mismatch between dissimilar electrodes generates mechanical stresses that degrade long-term stability.

### 1.1.2.2. Symmetrical cell

To address these limitations, the same material was applied to both electrodes. A cell with such electrodes is known as Symmetrical solid oxide cell (SSOC) with A/B/A structure and have been demonstrated to exhibit significant advantages over conventional SOCs, as illustrated in Figure 4B [32].

Unlike an asymmetric SOC, the count of electrode materials is limited to one. As a result, the screen-printing step is simplified, allowing the sintering of the electrode to be achieved in one thermal treatment. This approach could simplify the fabrication process and reduce associated costs. Moreover, it can alleviate the problems of chemical incompatibility and thermal mismatches. In addition, SSOCs are more convenient in practical applications because they eliminate the need to distinguish between the cathode and the anode [33].

However, these advantages are not universally applicable. While symmetrical designs have been demonstrated for specific materials (LSCM), they are commonly employed as a general commercial solution, and some electrodes' chemistries (e.g., certain SFM formulations) are impractical due to their instability under oxidizing and reducing conditions. In this work SSOCs are intentionally employed as a diagnostic tool to isolate and fingerprint the intrinsic processes of the PDC electrode, not primarily as proposed final cell architecture.

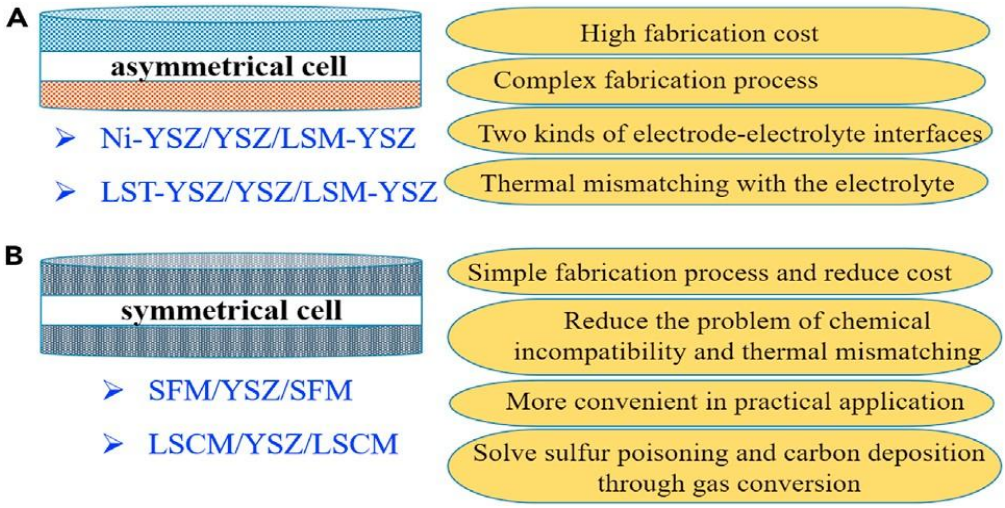


Figure 4: Comparison of solid oxide electrolysis cells, (A) Asymmetrical cell. (B) Symmetrical cell [33].

## 1.2. Fuel-Electrode Materials: From Ni-YSZ to MIECs

### 1.2.1. Ni-YSZ cermet

Ni-YSZ cermets remain the state-of-the-art anodes for SOFC and cathodes for SOEC because of their catalytic performance, electronic conductivity, and compatibility with YSZ electrolytes, although they face issues with their long-term stability.

In the Ni-YSZ electrode, the electrochemical reaction takes place at the Triple-Phase Boundary (TPB), where three phases meet: the Ni phase (which conduct electrons), the YSZ phase, and the gas-phase reactants (accessed through pores) [18]. These TPBs are essential areas for charge transfer, like $H_2$ oxidation or $CO_2$ reduction. Nonetheless, Ni agglomeration during elevated-temperature sintering compromises TPB integrity by enlarging Ni grains (~1μm), decreasing surface area (~$1 m^2 g^{-1}$) and constraining active sites for electrochemical reactions. This structural deterioration reduces efficiency with extended use [34]. While agglomeration directly affects the electrodes' microstructures, Ni's catalytic properties present further challenges when exposed to hydrocarbon fuels.

Ni catalyzes carbon deposition via hydrocarbon decomposition, forming graphite fibers that block active sites and induce mechanical stress, ultimately causing electrode deactivation and cell fracture [35]. These issues effectively impede the direct utilization of hydrocarbons in SOFCs and restrict the conditions that can be employed for $CO_2$ electrolysis in SOECs [36]. In addition to carbon deposition, trace contaminants like sulfur add further complexity to the stability of Ni-YSZ.

Exposure to trace sulfur (~1ppm $H_2S$) results in sulfur formation on the Ni surface, drastically degrading performance by blocking catalytic sites. Under typical conditions, sulfur adsorption is irreversible, necessitating sulfur tolerance modification [37]. Even when contaminants such as sulfur are mitigated, mechanical stresses from redox cycling further threatens the structural integrity of the electrode.

Ni-YSZ electrodes exhibit redox instability due to the re-expansion of metallic Ni upon reoxidation to NiO, which can fracture the electrode-electrolyte interface and damage the cell. This reoxidation occurs during shutdown procedures or near faulty seals (e.g., leaks), particularly under high $H_2O$: $H_2$ ratios and low temperatures, where Ni oxidation is thermodynamically favored [38].

### 1.2.2. Ni-YSZ stabilization and Modification

To mitigate these different challenges faced by conventional Ni-YSZ cermet, three modification strategies have emerged: infiltration of $CeO_2$ nanoparticles to enhance sulfur tolerance, as demonstrated by Kurokawa et al. [39]; alloying Ni with Cu or Sn to suppress carbon formation, pioneered via infiltration by Kim et al. [40] and extended to surface alloys by Nikolla et al. [41]; and protective coating such as Ru/ceria or LST layers to enable direct fuel reforming [42].

Despite the implementation of these stabilization and modification strategies, the fundamental drawbacks of Ni, namely agglomeration, carbon-induced deactivation, and redox-driven fracture, remain challenging to eliminate under realistic SOEC operation. Consequently, research has shifted towards entirely nickel-free mixed-ionic electronic conductors as alternative fuel electrode materials.

### 1.2.3. Nickel-Free MIECs

To circumvent the degradation mechanism inherent to Ni-based electrodes, such as agglomeration, migration, and carbon deposition under hydrocarbons/$CO_2$ feeds, nickel-free fuel electrodes have been identified as a possible solution, and consequently, they increase the stability of SOEC [43]. Two primary material families have emerged as the focus of research in this field: ceria-based MIECs (gadolinium (Gd)-doped ceria (GDC), or samaria (Sm-doped ceria (SDC)), which exhibit high ionic conductivity and redox stability under reducing conditions [44], and perovskite-based MIECs ($La_{0.75}Sr_{0.25}Cr_{0.5}Mn_{0.5}O_3$ (LSCM), $La_{0.20}Sr_{0.80}Ti_{0.90}Ni_{0.10}O_3$ (STFN), or $Sr_2Fe_{1.5}Mo_{0.5}O_6$ (SFM)), which offer tunable electronic conductivity and catalytic activity [45], [46].

## 1.3. Air-Electrodes Materials and Roles

The oxygen electrodes facilitate the oxidation of $O^{2-}$ ions to $O_2$ gas within the initial microns of the electrodes-electrolytes interfaces. To be considered suitable, an $O_2$ electrode must exhibit high mixed ionic-electronic conductivity, excellent electrocatalytic activity, and long-term chemical/thermal compatibility with the electrolyte. Given the propensity of Co-based perovskites (LSCF or LSC) to react with YSZ at operating temperatures, the implementation of an intermediate layer between the oxygen electrodes and YSZ is typically essential to impede interdiffusion and maintain the integrity of the interface [23].

Strontium-doped lanthanum manganite (LSM)-YSZ composites are a prevalent air electrode choice in SOECs. This can be attributed to the high electronic conductivity of LSM, its effective catalytic activity for the transformation of $O^{2-} \rightarrow O_2$ and its thermal expansion coefficient that closely matches that of YSZ. The synergy of these properties ensures remarkable long-term stability and minimal chemical reactivity between LSM and YSZ [47]. In such composites, YSZ provides ionic conduction, while LSM supplies both the electronic pathway and surface catalytic sites.

MIEC, such as $La_{0.6}Sr_{0.4}Co_{0.2}Fe_{0.8}O_{3-\delta}$ (LSCF) or $La_{0.6}Sr_{0.4}CoO_{3-\delta}$ (LSC), can also serve as air electrodes, since they enable fast $O^{2-}$ transport and improved surface-exchange kinetics.

However, because Co-perovskites form insulating secondary phases with YSZ above 750°C, a thin gadolinium-doped ceria (GDC) layer (0.1 -5 μm) is inserted between LSCF (or LSC) and YSZ to prevent these deleterious reactions [9].

### 1.4. Praseodymium Doped-Ceria (PDC) as Fuel-Electrode

While gadolinium-doped ceria has dominated as an MIEC electrolyte/electrode material, praseodymium doping offers better mixed conductivity and catalytic activity, critical advantages for symmetrical SOC operation [48]. This section examines why PDC is emerging as a transformative alternative to conventional Ni-YSZ and GDC systems.

#### 1.4.1. Crystal and Defect Chemistry

PDC adopts a fluorite crystal structure ($CeO_2$ lattice). Doping with praseodymium introduces oxygen vacancies ($V_O^{\bullet\bullet}$) via charge compensation mechanisms. Crucially, praseodymium exists in dual oxidation states ($Pr^{3+}$ and $Pr^{4+}$) under SOEC conditions, unlike fixed-valence dopants like $Gd^{3+}$.

The coexistence of $Pr^{3+}/Pr^{4+}$ also suppresses $Ce^{4+}$ reduction to $Ce^{3+}$minimizing electronic leakage in reducing environments, a key limitation of GDC electrolytes [49].

#### 1.4.2. Transport properties

The $Pr^{3+}/Pr^{4+}$ couple enables electron hopping under fuel electrode conditions (low $pO_2$), achieving mixed conductivity >0.01 S/cm at 700°C. This is critical for symmetrical cells, where both electrodes require bifunctional conductivity [48].

PDC's thermal expansion coefficient (TEC $\approx 10 - 11x10^{-6}$/K) closely matches zirconia electrolytes (TEC $\approx 12x10^{-6}$/K), reducing interfacial delamination risks during thermal cycling [50] [48].

#### 1.4.3. Surface reactivity

The surface chemistry of PDC features redox-active $Pr^{3+}/Pr^{4+}$ couples that drive distinct catalytic functions. $Pr^{4+}$ sites efficiently adsorb and dissociate oxygen molecules at the air electrodes, while $Pr^{3+}$ sites enable the incorporation of oxygen ions into the ceria latices. This dual functionality accelerates $H_2O/CO_2$ reduction kinetics during electrolysis and $O_2$ evolution during oxygen production [48].

Performance validation shows PDC electrodes achieve 0.17 Ω·cm² polarization resistance at 850°C - 30% lower than GDC equivalents, due to enhanced oxygen exchange coefficients ($k_{ex} = 3.2 \times 10^{-5}$ cm/s at 750°C) [48].

PDC significantly improves interfacial stability with zirconia electrolytes by suppressing undesirable reactions, such as $SrZrO_3$ formation. When deployed as an interlayer, PDC-based cells demonstrate exceptional durability with <2% performance degradation after 500 operational hours. This contrasts sharply with Ni-YSZ systems, which suffer >10% degradation under identical conditions due to redox instability and interfacial delamination [51].

### 1.5. Electrochemical Impedance Spectroscopy (EIS) and DRT Analysis

To investigate the sequence of processes that govern electrode performance, it is first necessary to review the fundamentals of EIS and equivalent circuit modeling (ECM), introduce the model-free Distribution of relaxation times (DRT) approaches, and finally demonstrate how DRT can help interpret data from EIS.

#### 1.5.1. EIS fundamentals

Electrochemical Impedance Spectroscopy (EIS) is a non-destructive technique used in electrochemistry to study the behavior of electrochemical systems by analyzing their impedance at different frequencies. It involves applying a small sinusoidal voltage perturbation $E(t) = E_0 \sin(\omega t)$, and measuring the resulting current $I(t) = I_0 \sin(\omega t + \emptyset)$. To define the complex impedance, the analysis is performed in the frequency domain by representing the sinusoidal signal with its complex amplitude [52].

$$\boldsymbol{Z^* = Z_0 e^{i\emptyset}} \quad 6$$

Utilizing Euler's renowned expression, $e^{j\emptyset} = \cos\emptyset + j\sin\emptyset$, the impedance $Z^*$ can be further simplified as the following equation:

$$\boldsymbol{Z_0(\cos\emptyset + j\sin\emptyset) = Z' + jZ''} \quad (7)$$

Where $Z'$ and $Z''$ are the real and imaginary components of the impedance, and $j = \sqrt{-1}$.

Impedance resistance is commonly depicted in Nyquist form, wherein the negative imaginary component of an impedance ($-Z''$) is plotted against its real components ($Z'$). Figure 5 shows a typical Nyquist Plot in SOCs' research, which is composed of one or more semicircles, with each semicircle corresponding to a distinct process occurring at a specific time scale [52]:

- High-frequency arc: its intercept at the real axis gives the ohmic resistance $R_\Omega$, arising from the electrolyte and contact resistances. The diameter of this first semicircle is often attributed to the charge-transfer resistance $R_{ct}$ at the electrode/electrolyte interface [18].
- Mid-frequency arc: this feature reflects surface-exchange kinetics (adsorption and incorporation of species), frequently modeled by a resistor in parallel with a constant-phase element (CPE, Q) to capture non-ideal capacitance due to surface heterogeneity [53].
- Low-frequency arc: its intercept at the real axis gives the polarization resistance $R_p$. A Warburg or Gerischer element appears at low frequencies, indicating diffusion-limited mass transport in the porous electrode or gas-phase boundary layer [54].

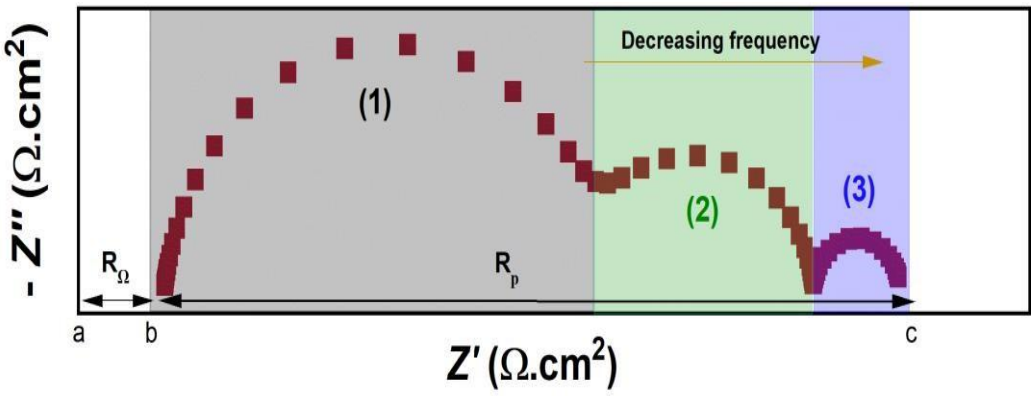


Figure 5: A typical Nyquist plot in SOCs' research, generated using the Relaxis® Circuit Simulator 3 [18].

To extract quantitative values for $R_\Omega$, $R_{ct}$, CPE parameters, and diffusion resistances, one fits the measured spectrum to an equivalent-circuit model using complex-nonlinear-least-squares (CNLS) regression. Common circuit elements include:

- R: ideal resistor
- Q: constant-phase element, impedance $Z_Q = (Q_0(j\omega^n))^{-1}$
- W: Warburg impedance for semi-infinite diffusion, $Z_W \sim (j\omega)^{-\frac{1}{2}}$
- G: Gerischer element for coupled kinetics-diffusion, $Z_G \sim (j\omega\tau)^{-\frac{1}{2}}$

By choosing the right combination of R, Q, W, and G, one can assign each observed arc or tail to its physical origin with electrochemical reaction [52], [55].

### 1.5.2. Distribution of Relaxation Times (DRT)

While ECM fitting works well when arcs are clearly separated, overlapping processes make element assignment ambiguous. The Distribution of Relaxation Times offers a model-free alternative by expressing the impedance as an integral over relaxation times τ:

$$\boldsymbol{Z^*(\omega) = R_\Omega + Z_p(\omega) = R_\Omega + R_p \int_0^\infty \frac{\gamma(\tau)}{1 + j\omega\tau} d\tau} \quad (8)$$

With $\int_0^\infty \gamma(\tau)\, d\tau = 1$

Where $Z^*(\omega)$ is the impedance data, $R_\Omega$ is the ohmic resistance, $R_p$ is the polarization resistance and $Z_p$ is the polarization component of the impedance.

It is imperative to transform the second term of the equation (8) with $\gamma(\tau)$ to calculate the DRT of a specific impedance. However, this poses an ill-posed problem [56]. To address these issues, a range of methodologies have been proposed [57], with the Tikhonov-regularization approach emerging as a particularly effective solution. During the adaptation process, selecting an appropriate regularization parameter (λ) is crucial to avoid misinterpreting the data, particularly when comparing different spectra. To further elucidate the matter, it must be noted that if a high λ value is selected for DRT, this could result in the merging or broadening of the DRT peaks. Conversely, if a low λ value is chosen, then this can create several false peaks, mainly due to the measurement noise [58].

The DRT plot graphically represents $g(\tau)$ against relaxation time (τ) or frequency (f), typically revealing multiple peaks at varying relaxation times. However, a common assumption is that each peak corresponds to a specific time constant and represents an electrode process physically. This theory applies to the circuit element of the R-C and CPE varieties. In the DRT plot, the R-C element is represented by a Dirac pulse, and the CPE element is represented by a broader peak with a Gaussian distribution [59]. In contrast, this assumption does not apply to a circuital element such as Warburg, the transmission line model, and the Gerischer model, which exhibit multiple smaller peaks at lower relaxation times alongside a primary peak [60]. Figure 6 corresponds to the DRT spectra of the Nyquist plot, which is visualized in Figure 5. It is noteworthy that the number of time constants contributing to the Nyquist plot manifests as discrete peaks in the DRT spectrum.

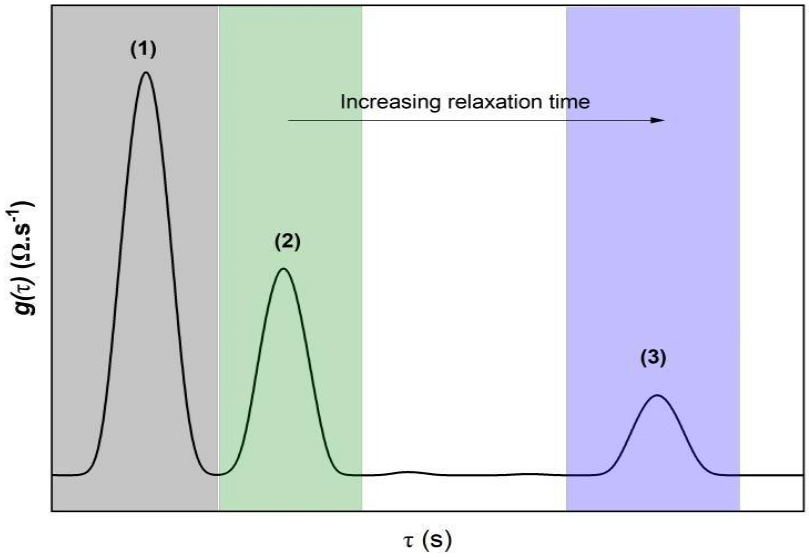


Figure 6: Distribution of Relaxation Times (DRT) corresponding to the Nyquist plot, visualised in Figure 5 [18].

### 1.5.3. Identifying the Rate-Determining Step

Once the DRT spectrum $\gamma(\tau)$ is obtained, the resistive contribution $R_i$ of each relaxation process i is calculated as [61]:

$$\boldsymbol{R_i = R_p \int_{\tau i-}^{\tau i+} \gamma(\tau)\, d\tau} \tag{9}$$

Where the integral gives the normalized fraction of $R_p$ for that peak. Because $\sum_i \int_0^\infty \gamma(\tau)\, d\tau = 1$, the individual $R_i$ sum to the total resistance, $\sum_i R_i = R_p$.

The rate-determining step is identified as the peak with the largest $R_i$.

To validate this assignment, one can use:

- Temperature scans (Arrhenius analysis)

Plot ln ($R_i$) versus 1/T to extract activation energies $E_a$. Different physical processes (charge transfer vs surface exchange) exhibit distinct $E_a$ values, confirming the nature of each peak.

- Gas-composition $p(O_2)$ variation

By measuring DRT under different oxygen partial pressures or fuel-oxidant ratios, one tracks how each $R_i$ shifts with $pO_2$. A process that is surface-exchange limited will show a different $pO_2$-dependence than one limited by bulk diffusion [43].

## 1.6. Symmetrical-Cell Methodology for Electrode Kinetics

### 1.6.1. Why use a symmetrical cell?

Conventional, asymmetric SOECs exhibit overlapping low-frequency arcs that emerge concurrently at the fuel and air electrodes, making it difficult to discern the kinetics of the fuel side from those of the air side. The implementation of the same materials on both sides of a single cell (PDC/GDC/YSZ/GDC/PDC) results in an inherently symmetrical cell, wherein each Nyquist feature is exclusively attributable to fuel electrode processes. This method greatly simplifies DRT and equivalent circuit analysis, thereby providing unambiguous kinetic fingerprints for adsorption, charge transfer, and diffusion on the PDC [32], [62].

### 1.6.2. Working Principles of a single-chamber symmetrical cell

Figure 7 shows how a typical symmetrical solid oxide cell works. When the cell is operating in electrolysis mode (fed with $H_2/H_2O$), steam is split, water molecules pick up electrons, and produce $H_2$ while releasing oxide ions into the solid electrolyte. $O^{2-}$ migrates through the electrolyte to the opposite electrode. Once at the opposite electrodes, oxide ions are consumed (fuel cell mode): $O^{2-}$ reacts with $H_2$, releasing electrons back to the external circuit. The net chemistry and the direction of electron flow depend on the applied potential and the gas compositions at each side.

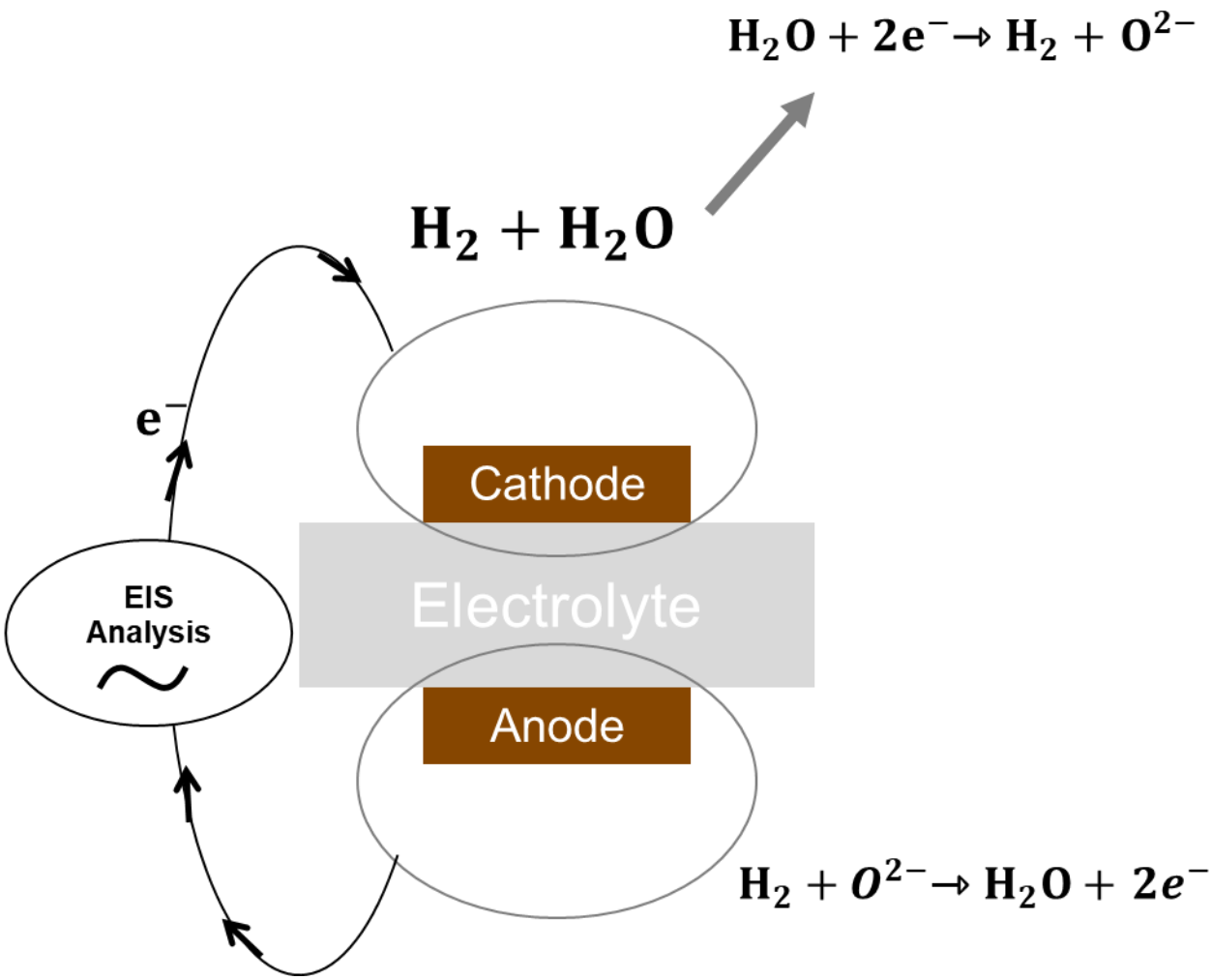


Figure 7: Working Principles of symmetrical solid oxide cell

### 1.6.3. Literature Example

Some pioneering work on symmetric cells concentrated on mixed-conducting perovskites is presented here:

- Bastidas et al. (2006) fabricated $La_{0.75}Sr_{0.25}Cr_{0.5}Mn_{0.5}O_3$/YSZ/$La_{0.75}Sr_{0.25}Cr_{0.5}Mn_{0.5}O_3$ symmetrical cell. On wet $H_2$ at 900 °C, they achieved a peak power density of 300mW.$Cm^{-2}$ and demonstrated excellent redox stability [63].
- Ruiz-Morales et al. (2011) introduced polymethyl methacrylate (PMMA) templating to create controlled porosity in LSCM electrodes. Their symmetrical cells achieved 800mW.$cm^{-2}$ in $H_2$ and 500mW.$cm^{-2}$ $CH_4$ at 950 °C, highlighting both high performance and full reversibility between fuel cell and electrolysis modes [62].
- Bumberger et al. (2024) developed the rigorous one-dimensional transmission-line + DRT framework for mixed-conducting electrodes, including symmetric geometries. They showed how to map impedance spectra of dense GDC/YSZ/GDC cells onto a

physically derived circuit to cleanly separate bulk ionic/electronic conduction from interfacial charge-transfer processes, thereby enabling unambiguous rate-determining-step identification [53].

### 1.6.4. Limitations and PDC knowledge gap

Despite clear advantages demonstrated by perovskite-based MIEC (LSCM) and ceria-based MIEC (GDC) symmetric cells in isolating electrode kinetics via EIS/DRT, no symmetrical cell study has yet examined praseodymium-doped ceria (PDC), leaving its kinetic behavior uncharted in this format.

### Conclusion

This literature review has comprehensively examined the fundamental principles, materials advancements, and electrochemical characterization techniques central to solid oxide cells, emphasizing the thermodynamic imperative for high-temperature operation (600 °C to 1000 °C) to enhance ionic conductivity, accelerate kinetics, and leverage waste heat for reduced electrical energy demand. Critical analysis reveals the limitations of traditional Ni-YSZ fuel electrodes, which are susceptible to agglomeration, carbon deposition, and sulfur poisoning. In contrast, symmetrical cell architecture is highlighted for its simplicity in fabrication, interfacial stability, and unique utility in isolating electrode kinetics via electrochemical impedance spectroscopy (EIS) and distribution of relaxation times (DRT) analysis. The emergence of Nickel-free mixed-ionic electronic conductors (MIECs), particularly praseodymium-doped ceria (PDC), was underscored for its superior ionic transport, redox-active catalysis, and compatibility with zirconia electrolytes, positioning it as a transformative material for symmetrical SOCs. This comprehensive literature review provides a foundation for future research and development in the field of SOC, with a focus on efficiency and durability through material innovation. The subsequent chapter details the experimental methodologies, including symmetrical cell fabrication, electrochemical testing protocols, and DRT interpretation, employed to validate these strategies.

# CHAPTER 2: MATERIALS AND METHODS

# Chapter 2: MATERIALS AND METHODS

## Introduction

This chapter provides a detailed explanation of how the study was conducted and the materials and methods used for the electrochemical characterization of the symmetrical PDC10 electrode.

## 2.1. Study area

This experimental study was conducted in the High Temperature Electrochemistry department, IET-1, at Forschungszentrum Jülich in Germany.

## 2.2. Symmetrical cell preparation

The symmetrical cells (Figure 8) were prepared using a commercial 8YSZ (8 mol% yttria-stabilized zirconia) electrolyte support (Kerafol®, thickness 250 µm, diameter 20 mm). A GDC barrier layer $Ce_{0.8}Gd_{0.2}O_{0.1}$ prepared from CerPoTech powder, screen-printed on both faces of the electrolyte to a thickness of approximately 3 µm, was used to inhibit interdiffusion between the electrolyte and electrode, and to avoid any possible reaction of PDC10 with 8YSZ electrolyte. The $Pr_{0.1}Ce_{0.9}O_{2-\delta}$ (PDC10) electrode paste was then screen printed atop the GDC layer. Au current collector was included on the outer faces to improve electronic conductivity. Post-deposition, the cell was sintered, resulting in the final Au/PDC10/GDC/8YSZ/GDC/PDC10/Au configuration. Two versions were examined: cell A with combined GDC + PDC10 thickness of around 46 µm, and cell B with thickness of about 19 µm.

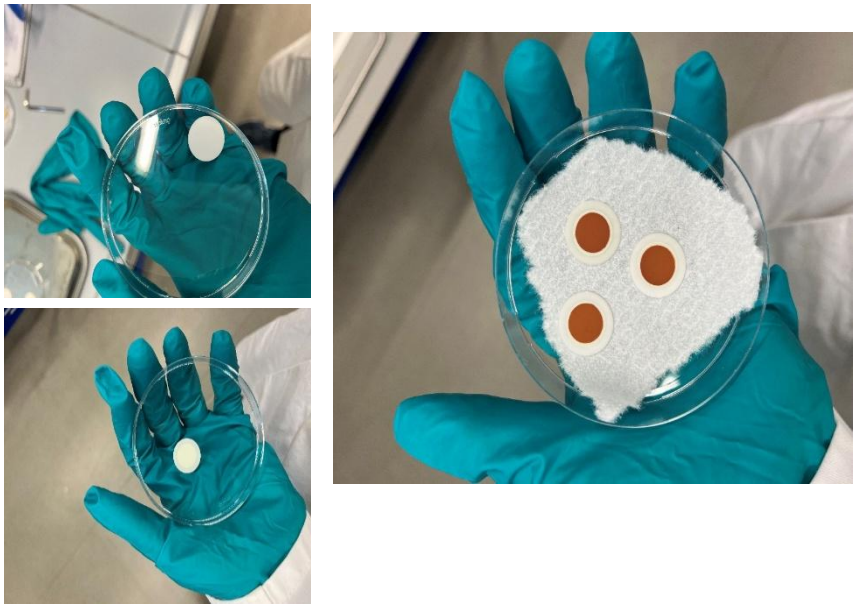

Figure 8: Layered components of the symmetric PDC/GDC/8YSZ/GDC/PDC cell

### 2.3. Cell conditioning

The symmetrical Au/PDC10/GDC/8YSZ/GDC/PDC10/Au button cells were mounted in a NorECs® (Norwegian Electro Ceramics®, NORECS, Oslo, Norway) probostat equipped with a Carbolite Gero® (Neuhausen, Germany) tube furnace (Figure 9). A platinum rod inserted through the ceramic support tube served as an inner current collector on one face of the cell, while a gold mesh on the opposite face acted as the outer current collector. Gold ring gaskets placed between the inner face and the ceramic holder provide a gas-tight seal, and a spring-loaded clamp maintains uniform compressive force to ensure stable electrical contact throughout the procedure.

Once assembled, the cell was heated from ambient temperature to 900 °C at a controlled ramp rate of $2^{o}\mathrm{C}.\,\mathrm{min}^{-1}$ and a gas composition of $6\ \mathrm{Nl}\cdot\mathrm{h}^{-1}$ of Nitrogen ($\mathrm{N}_2$).

Upon reaching 900 °C, the cell was then reduced following two steps. The initial reduction involved switching to $6\ \mathrm{Nl}\cdot\mathrm{h}^{-1}$ of forming gas ($5\%\mathrm{H}_2$ in $\mathrm{N}_2$). For the second step, it was switched to a wet-reduced atmosphere $50\%\mathrm{H}_2\mathrm{O}$-$50\%\mathrm{H}_2$ with a total volume flow of $9\ \mathrm{Nl}\cdot\mathrm{h}^{-1}$, which was maintained for an additional hour for the cell to be fully reduced and stable [43].

Immediately following the equilibrium, electrochemical impedance spectroscopy was performed at zero net bias under the wet $50\%\mathrm{H}_2\mathrm{O}$-$50\%\mathrm{H}_2$ atmosphere at 900 °C. A 50 mV AC perturbation was applied over the frequency range from 11 kHz down to 0.11 Hz, and the resulting current oscillations were constrained within ± 500 µA. Measurements were recorded with an Ivium Vertex.5 potentiostat/galvanostat, ensuring that both the PDC10 electrodes and GDC barriers were fully activated and stable in the wet reducing environment before any further electrochemical tests.

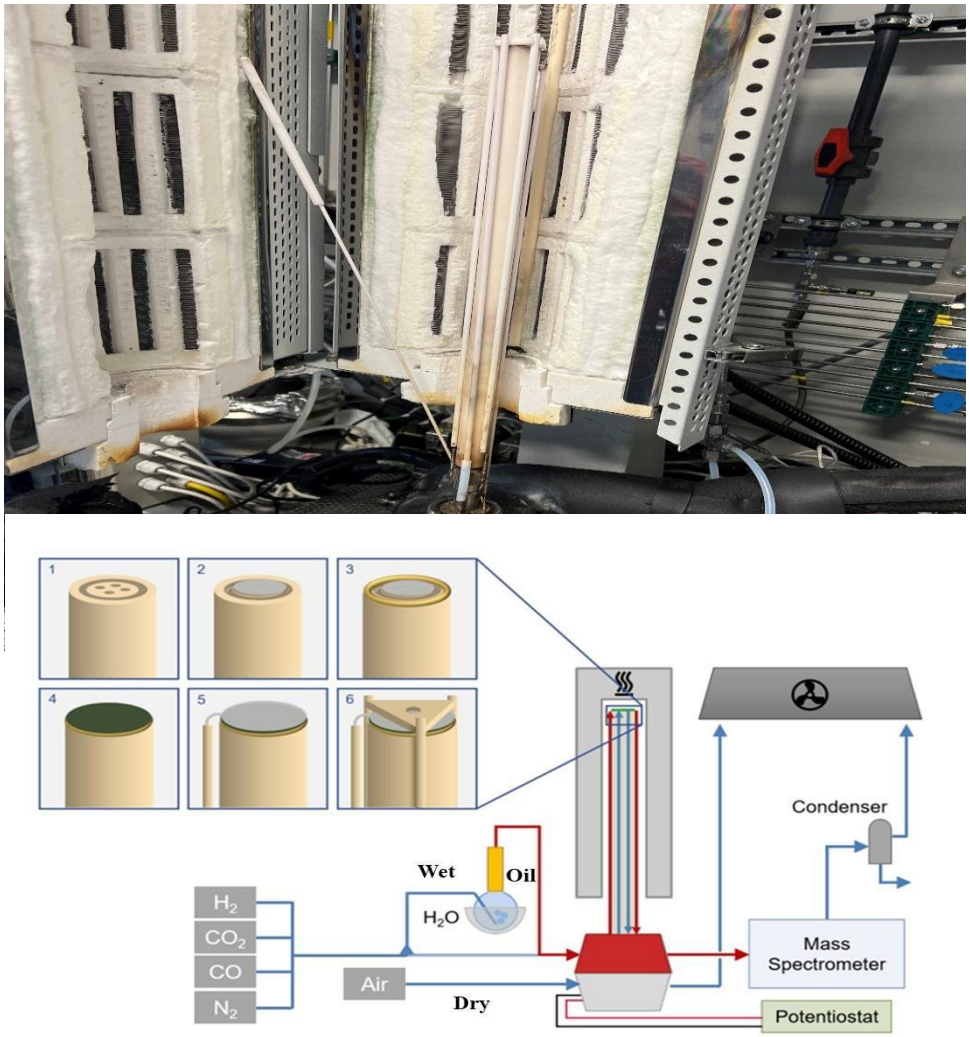


Figure 9: Test rig and Schematic diagram of the experimental setup [26].

## 2.4. Electrochemical characterization

Electrochemical impedance spectroscopy (EIS) evaluated the electrochemical characterization processes involving the fully reduced symmetrical cells as a function of both temperature and gas composition. Measurements were carried out under a constant open circuit voltage (OCV) condition, with both faces of the cell exposed to identical atmospheres.

A small AC perturbation of 50 mV was applied over the frequency range 11 kHz to 0.11 Hz, with 21 frequencies per decade. No DC bias or I-V sweeps were performed, since the symmetrical cell configuration does not support net fuel-cell or electrolysis currents [43].

Impedance data were transferred to OriginPro 2024 for initial plotting and baseline adjustment. Thereafter, distribution-of-relaxation-times (DRT) and equivalent circuit model (ECM) evaluation were performed with the Relaxis® software developed by RHD-Instruments.

### 2.4.1. Temperature variation

In our experiments, the steam content was controlled exclusively by adjusting the oil-bath temperature, while all other conditions (flow rates, temperature ramp, frequency ranges, and AC amplitudes) remained identical. For the first symmetrical cell (46 µm), we generated a $50\%H_2O$-$50\%H_2$ mixture by keeping the oil bath to 84 °C and feeding $4.5\ Nl \cdot h^{-1}H_2$. With the furnace at 900 °C, impedance spectra were recorded, and then the temperature was lowered in 25 °C steps down to 750 °C, allowing 30 min of equilibrium at each point before measurement. The same protocol was repeated at $70\%H_2O$-$30\%H_2$ (oil bath 90 °C, $2.7\ Nl \cdot h^{-1}\ H_2$) and $90\%H_2O$-$10\%H_2$ (oil bath 96 °C, $0.9\ Nl \cdot h^{-1}\ H_2$) to investigate the effect of increased steam activity [43].

The second symmetrical cell (19 µm) followed the same thermal sweep from 900 °C down to 750 °C in 25 °C increments, at a rate of $2°C.min^{-1}$, with a 30 min hold in five different gas compositions (Table 1). Using this information, we developed a high-resolution dataset that shows the impact of electrode/barrier thickness on cell performance.

Table 1: Impedance measurement condition cell B under varied $H_2O/H_2$ mixture

| **Steam% / $H_2$%** | **Oil-bath T (°C)** | **$H_2$ flow ($Nl \cdot h^{-1}$)** | **Temp. sweep (°C)** | **Ramp rate** | **Hold time** |
|---|---|---|---|---|---|
| 10 /90 | 46 | 8.1 | 900 → 750 | $2°C.min^{-1}$ | 30 min |
| 30 / 70 | 70 | 6.3 | 900 → 750 | $2°C.min^{-1}$ | 30 min |
| 50 /50 | 84 | 4.5 | 900 → 750 | $2°C.min^{-1}$ | 30 min |
| 70 / 30 | 90 | 2.7 | 900 → 750 | $2°C.min^{-1}$ | 30 min |
| 80 / 20 | 94 | 1.8 | 900 → 750 | $2°C.min^{-1}$ | 30 min |

### 2.4.2. Gas variation

In this set of experiments, the cell temperature was initially held constant at 900 °C, then at 800 °C for the first cell, while varying the gas composition. Two different sweeps were performed at each temperature (Table 2):

- $H_2O$-constant sweep ($H_2O$ = 4.5 Nl·h⁻¹; $H_2$ = 4.5 Nl·h⁻¹): $N_2$ was increased stepwise from 0 to 3.6 Nl·h⁻¹, reducing $H_2$ accordingly to maintain total flow of 9 Nl·h⁻¹
- $H_2$-constant sweep ($H_2$ = 4.5 $Nl \cdot h^{-1}H_2O$): $N_2$ were varied to adjust steam fraction, with oil-bath temperatures chosen to achieve the target $H_2O$ partial pressures.

Impedance spectra were recorded at each gas composition after 10 min of equilibrium. The same protocol was then applied for the second symmetrical cell at 900 °C and 850 °C.

Table 2: Flow rate and oil bath setting for gas variation experiment

| **$H_2O$-constant** | | | | | |
|---|---|---|---|---|---|
| **$N_2$ flow (Nl·h⁻¹)** | **Steam%** | **Oil-bath T (°C)** | **$H_2$ flow (Nl·h⁻¹)** | **Temp (°C)** | **Hold time** |
| 0 | 50 | 84 | 4.5 | 900, 850 (B), 800(A) | 10 min |
| 0.9 | 50 | 84 | 3.6 | 900, 850 (B), 800(A) | 10 min |
| 1.8 | 50 | 84 | 2.7 | 900, 850 (B), 800(A) | 10 min |
| 2.7 | 50 | 84 | 1.8 | 900, 850 (B), 800(A) | 10 min |
| 3.6 | 50 | 84 | 0.9 | 900, 850 (B), 800(A) | 10 min |
| **$H_2$-constant** | | | | | |
| 0 | 50 | 84 | 4.5 | 900, 850 (B), 800(A) | 10 min |
| 0.9 | 40 | 76 | 4.5 | 900, 850 (B), 800(A) | 10 min |
| 1.8 | 30 | 70 | 4.5 | 900, 850 (B), 800(A) | 10 min |
| 2.7 | 20 | 61 | 4.5 | 900, 850 (B), 800(A) | 10 min |
| 3.6 | 10 | 46 | 4.5 | 900, 850 (B), 800(A) | 10 min |

## Conclusion

This chapter has described the fabrication of the symmetrical Au/PDC10/GDC/8YSZ/GDC/PDC10/Au button cell variants (46 and 19 micrometers) on commercial 8YSZ supports along with their two-stage high-temperature reduction in forming gas and controlled wet $H_2/H_2O$, and the detailled EIS protocols used to probe their impedance behavior. We have outlined how steam content was tuned via oil-bath temperature, how temperature sweeps (900 → 750 °C) and gas composition matrices were implemented at zero bias, and how data were analyzed. The following chapter will present these impedance spectra and discuss how electrode thickness, temperature, and steam-hydrogen ratios govern the electrochemical performance of the symmetrical PDC cells.

# CHAPTER 3: RESULTS AND DISCUSSION

# Chapter 3: RESULTS AND DISCUSSIONS

## Introduction

To further investigate the performance of our symmetrical PDC10 cells, we employed several complementary techniques, including scanning electron microscopy (SEM) for microstructure characterization, Arrhenius analysis, and distribution of relaxation times (DRT) analysis, along with equivalent circuit fitting.

## 3.1. Microstructure characterization (SEM)

Scanning electron microscopy (SEM) was performed on both versions of the PDC10/GDC/8YSZ/GDC/PDC10 cells to establish their baseline microstructures. As demonstrated by Figure 10 and Figure 11, both 46 µm and 19 µm PDC10 films form well-connected porous networks.

In cross-section, every PDC10 layer remains tightly bonded to the 3 µm GDC barrier below, showing no sign of delamination or cracking at the interface. In both samples, the 250 µm 8YSZ is crack-free and the GDC barrier is intact, validating that our sintering procedure maintains the overall structural integrity.

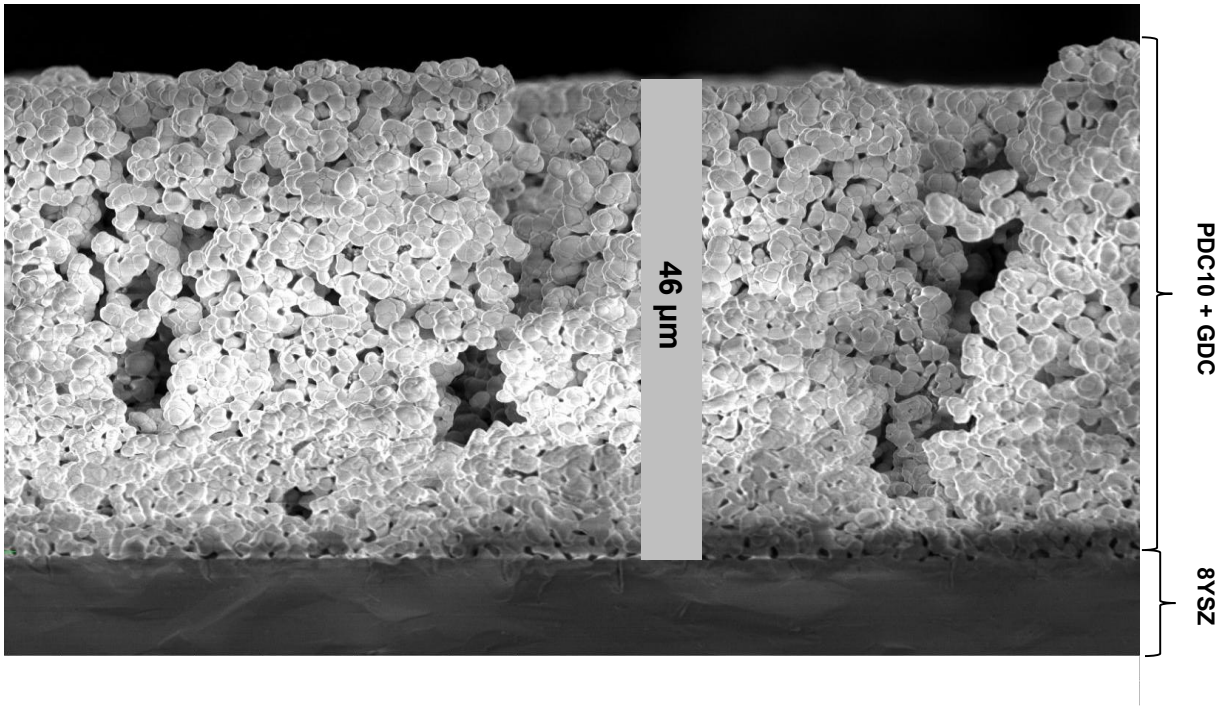


Figure 10: Scanning electron microscopy (SEM) cross-section image of 46 µm PDC10

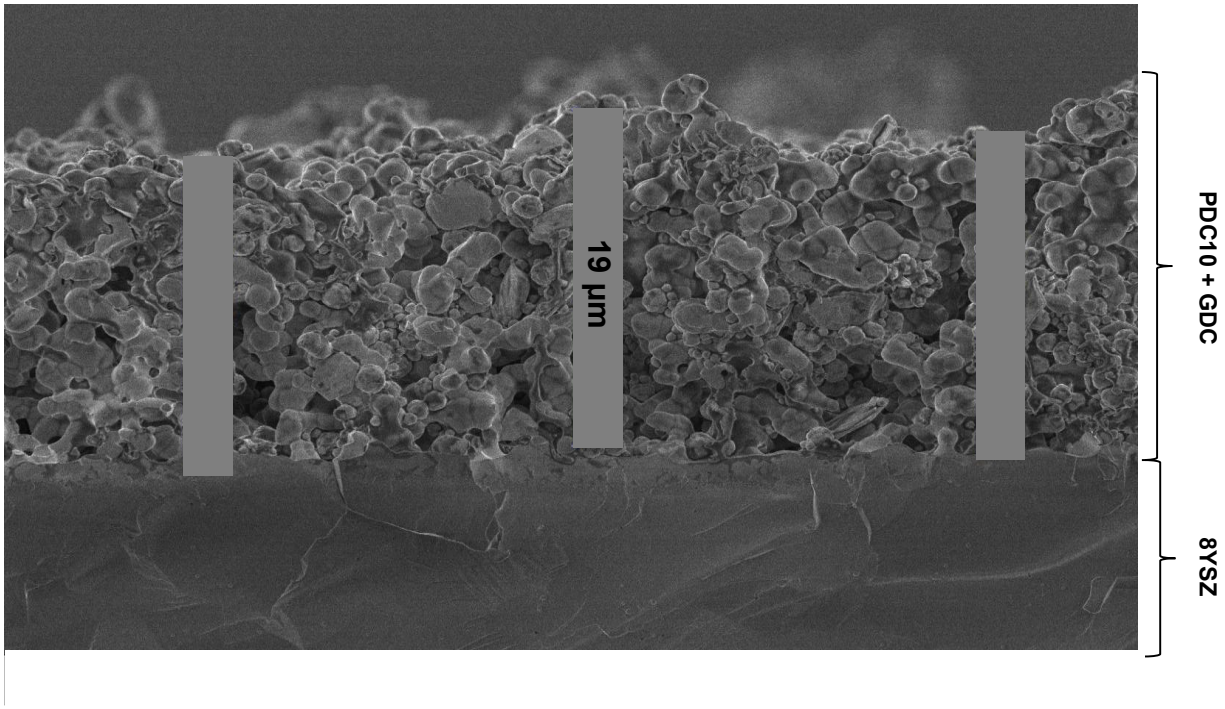


Figure 11: Scanning electron microscopy (SEM) cross-section image of 19 µm PDC10

With this baseline microstructural picture in hand, we now turn to electrochemical impedance spectroscopy to see exactly how these pores affect each cell's ohmic and polarization resistances.

### 3.2. Electrochemical impedance spectroscopy

#### 3.2.1. Nyquist plot comparison at 850 °C, 50%$H_2O$+50%$H_2$

To further evaluate the electrochemical performance of the two symmetrical PDC10 cells, impedance data were taken from 900 °C down to 750 °C under steam electrolysis conditions (50%$H_2O$+50%$H_2$). As illustrated in Figure 12, the resulting Nyquist plots are displayed for both 46 µm and 19 µm thick electrodes at 850 °C. Each cell presents a single, depressed semicircle, a characteristic response for symmetrical solid oxide cells, where the high frequency intercept corresponds to the ohmic resistance ($R_\Omega$) and the arc diameter corresponds to the area specific resistance (ASR).

Quantitatively, the 46 µm cell exhibits an $R_\Omega$ of 0.43 Ω and a total ASR of 1.17 Ω.Cm$^2$, with Rp accounting for 0.29 Ω.cm$^2$, calculated using equation 10. In comparison, the 19 µm cell shows improved performance with an $R_\Omega$ of 0.37 Ω, an ASR of 1.05 Ω.cm$^2$, and a reduced Rp of 0.26 Ω.Cm$^2$. These reductions, about 13% in ohmic resistance and 9% in polarization resistance, show how the thickness of the electrodes affects the electrochemical behavior of the cell. Thinner electrodes generally offer shorter ionic transport paths and may contribute to more efficient charge transfer and gas diffusion [64].

$$\mathbf{Rp} = \left(\frac{\boldsymbol{ASR} - \boldsymbol{R_\Omega}}{\mathbf{2}}\right) * \mathbf{0.735} \tag{10}$$

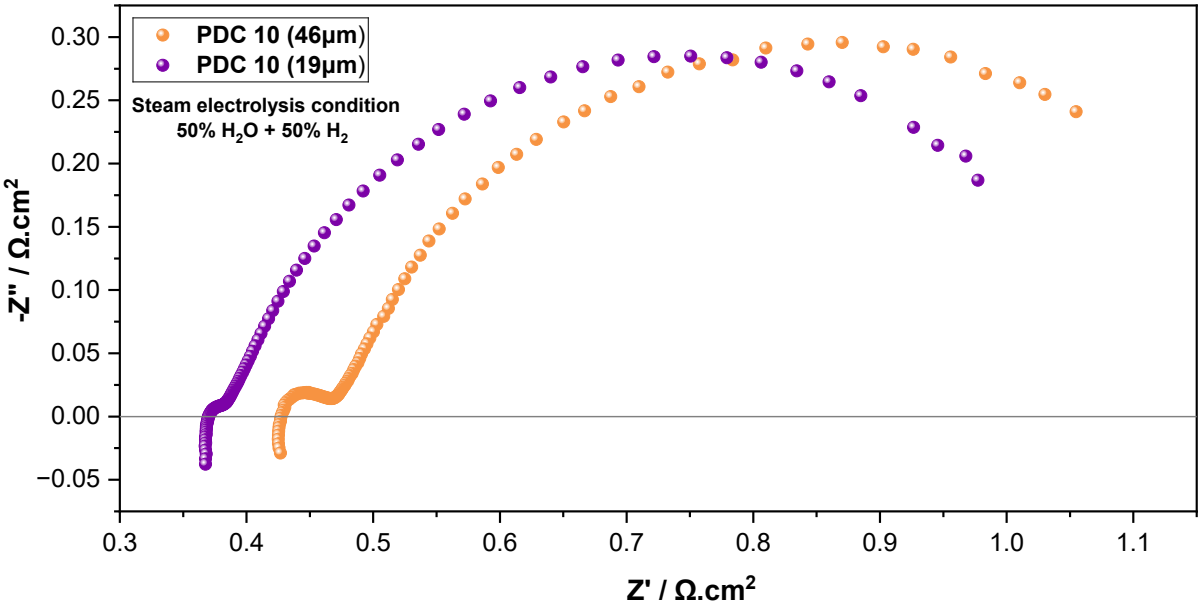


Figure 12: Nyquist plot of symmetrical PDC10 cells during steam electrolysis at OCV, with a composition of 50% $H_2$ and 50% $H_2O$, at 850 °C

Based on the improved polarization resistance, the 19 µm PDC10 cell was selected for subsequent in-depth analysis using the distribution of relaxation times and equivalent circuit modeling.

### 3.2.2. Temperature dependence (Arrhenius analysis)

To quantify the responses of both ohmic and polarization resistances to temperature, Arrhenius plots were constructed from the EIS data collected at temperatures ranging from 750 °C to 900 °C.

Figure 13 presents the Arrhenius plots of the ohmic resistance $R_\Omega$ of the selected 19 µm PDC10 as ln ($R_\Omega$) versus 1/T for five steam-hydrogen ratios (10%-80% $H_2O$) between 750 °C and 900 °C. In every gas mixture, ln ($R_\Omega$) rises linearly with 1/T. Despite the slight vertical offsets among the five curves, there is no systematic trend in $R_\Omega$ as a function of steam content. Based on these data, it has been concluded that under these conditions, the ohmic resistance is insensitive to steam concentration.

Figure 14 shows the Arrhenius plots for the total polarization resistance Rp across the 750 °C - 900 °C range under the five $H_2O$-$H_2$ mixtures, and it is immediately apparent that the points do not fall on clear, parallel straight lines as it has been seen for the ohmic resistance, and do not show any clear dependence on the steam-hydrogen composition.

Displaying the same data as a bar chart in Figure 15 makes the lack of a clear trend even further. From 900 °C to 850 °C, a slight but steady decrease in Rp is observed as the steam concentration decreases from 10%-80%. Nonetheless, between 825 °C and 750 °C, the Rp values for 30%, 50%, and 70% $H_2O$ stay nearly unchanged, while the curves for 80% and 10% intersect.

In Figure 16, the Arrhenius plots of the ohmic and polarization resistances at 50% $H_2$ + 50% $H_2O$ have been displayed, thereby yielding an activation energy of 80.84 $kJ.mol^{-1}$ for the ohmic resistance, which is close to 88 $kJ.mol^{-1}$ reported in the literature for YSZ electrolytes [65], [66]. This confirms that the main part of the ohmic resistance is contributed by the 8YSZ electrolyte (250 µm). The polarization resistance Rp shows a slightly lower activation energy of 98.94 $kJ.mol^{-1}$ due to a shorter diffusion path compared to the 107 $kJ.mol^{-1}$ reported for a symmetrical GDC fuel electrode in steam electrolysis conditions [44].

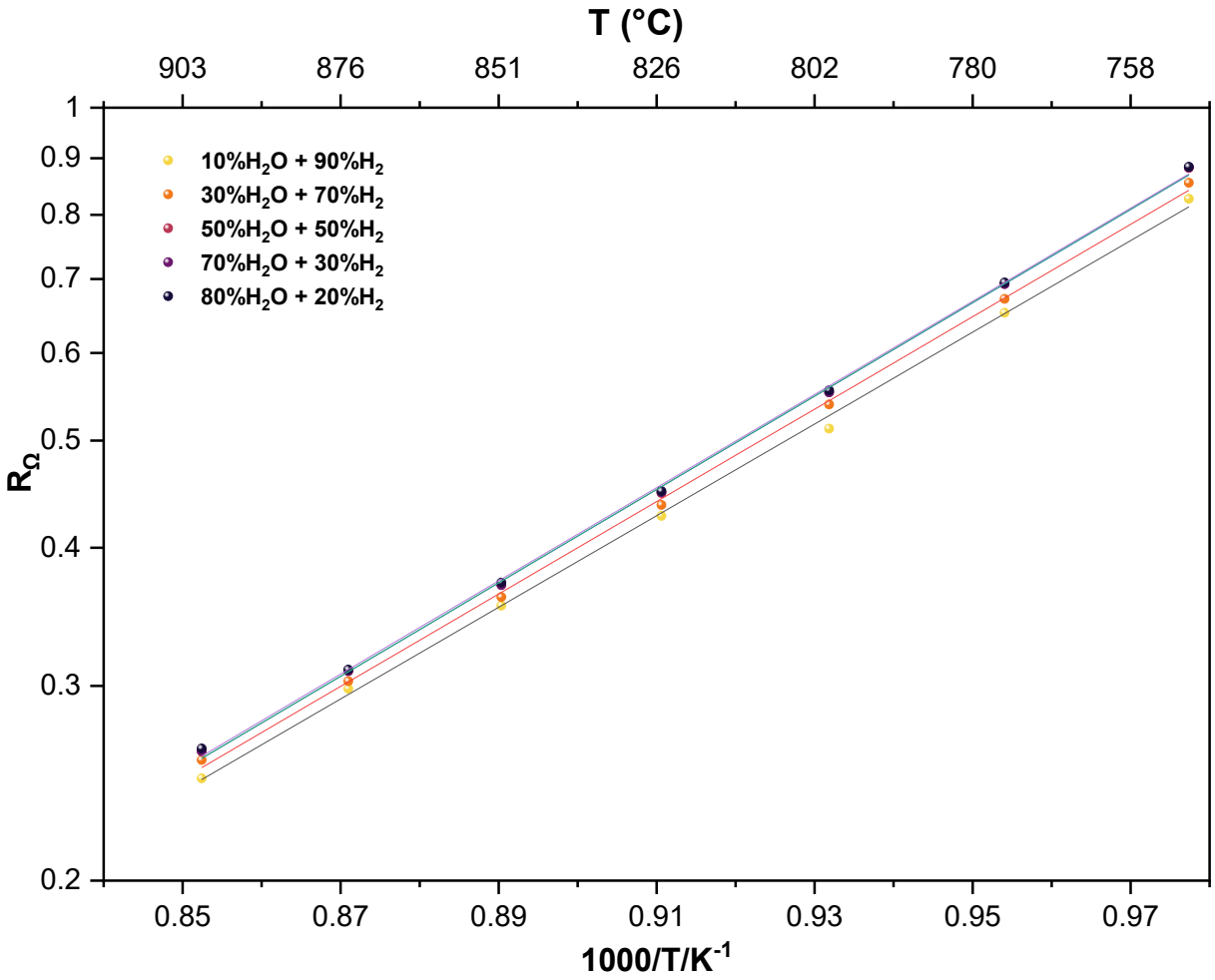


Figure 13: Arrhenius plots of the ohmic resistance with the five steam-hydrogen mixtures

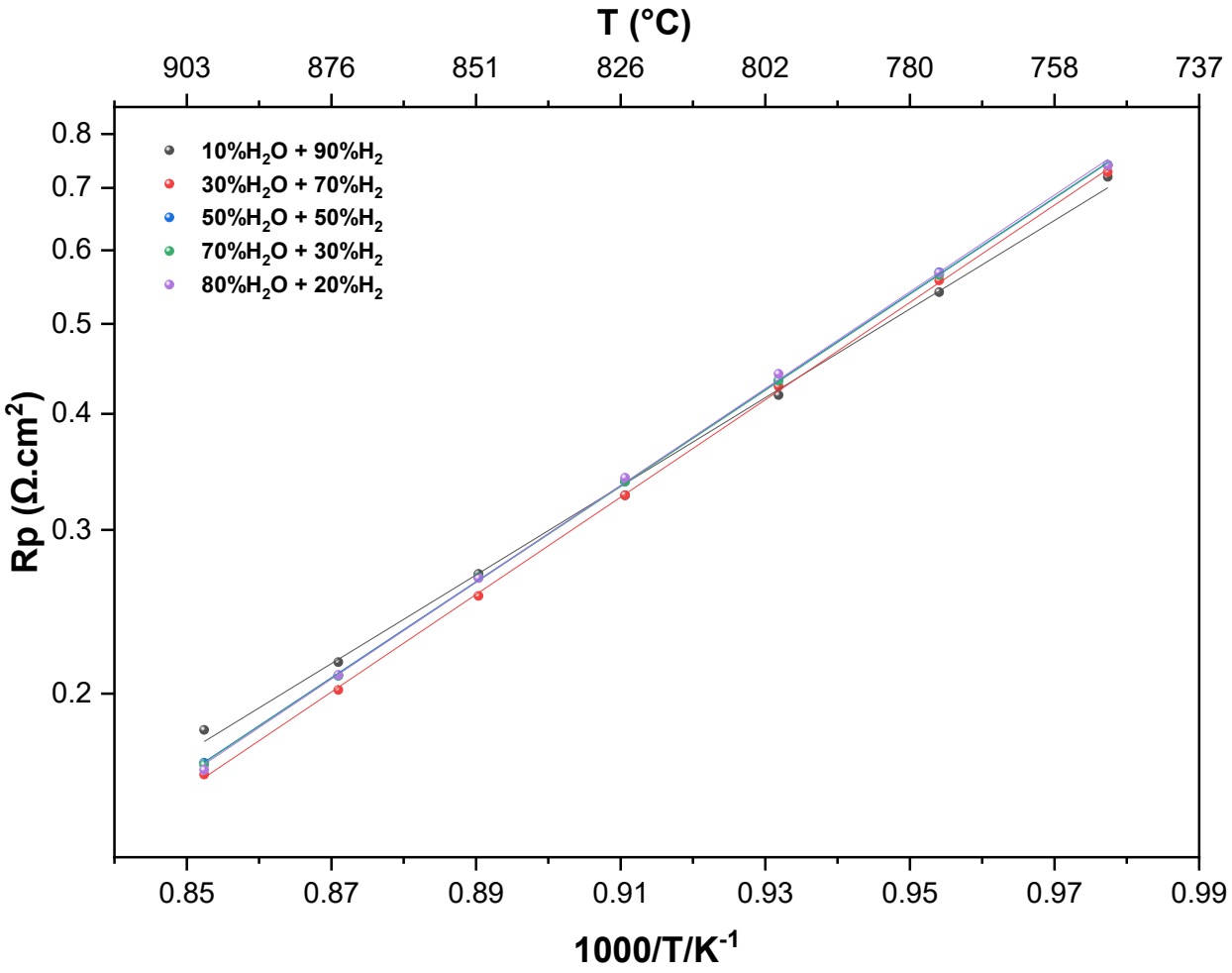


Figure 14: Arrhenius plots of the polarization resistance with the five steam-hydrogen mixtures

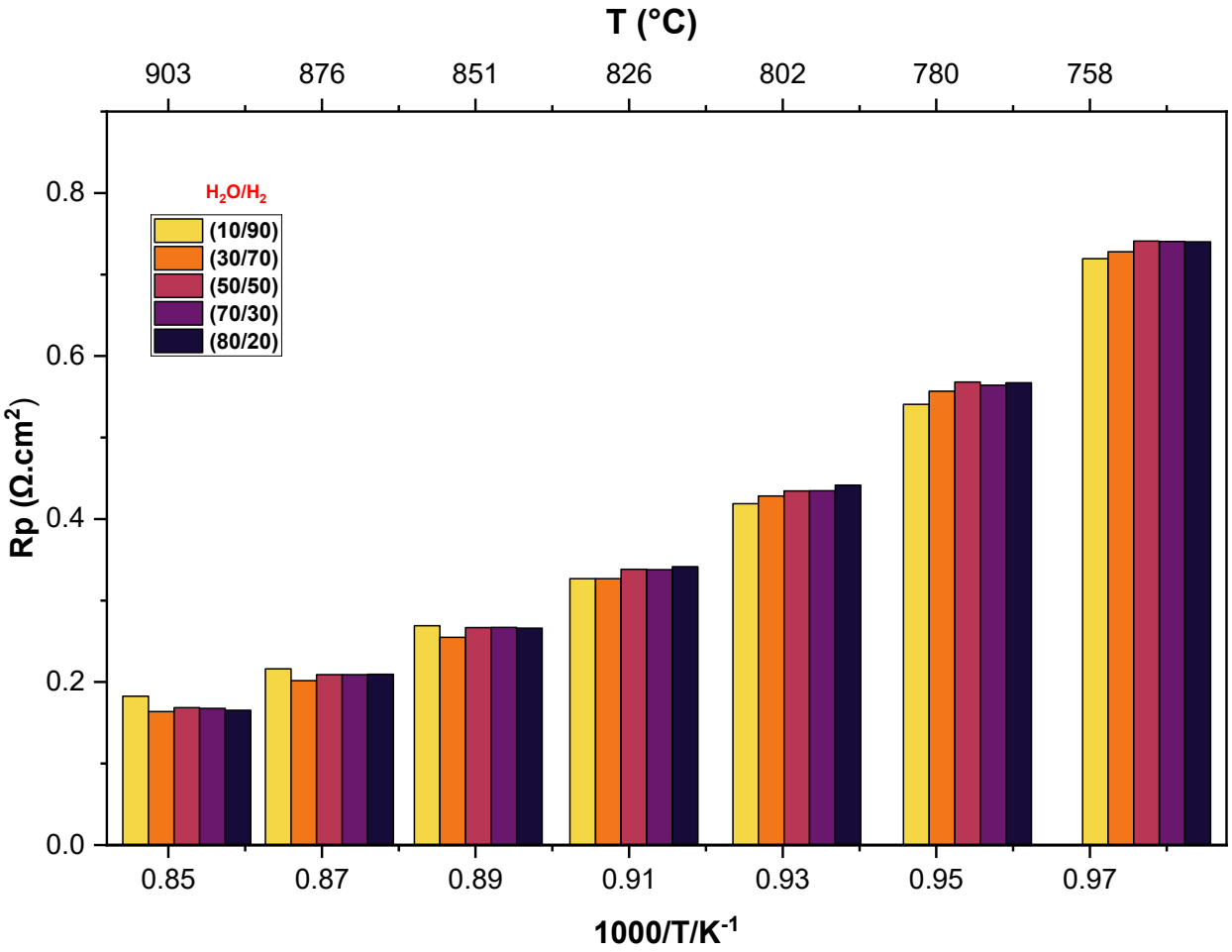


Figure 15: Bar chart of the Arrhenius plots of the polarization resistance with the five steam-hydrogen mixtures

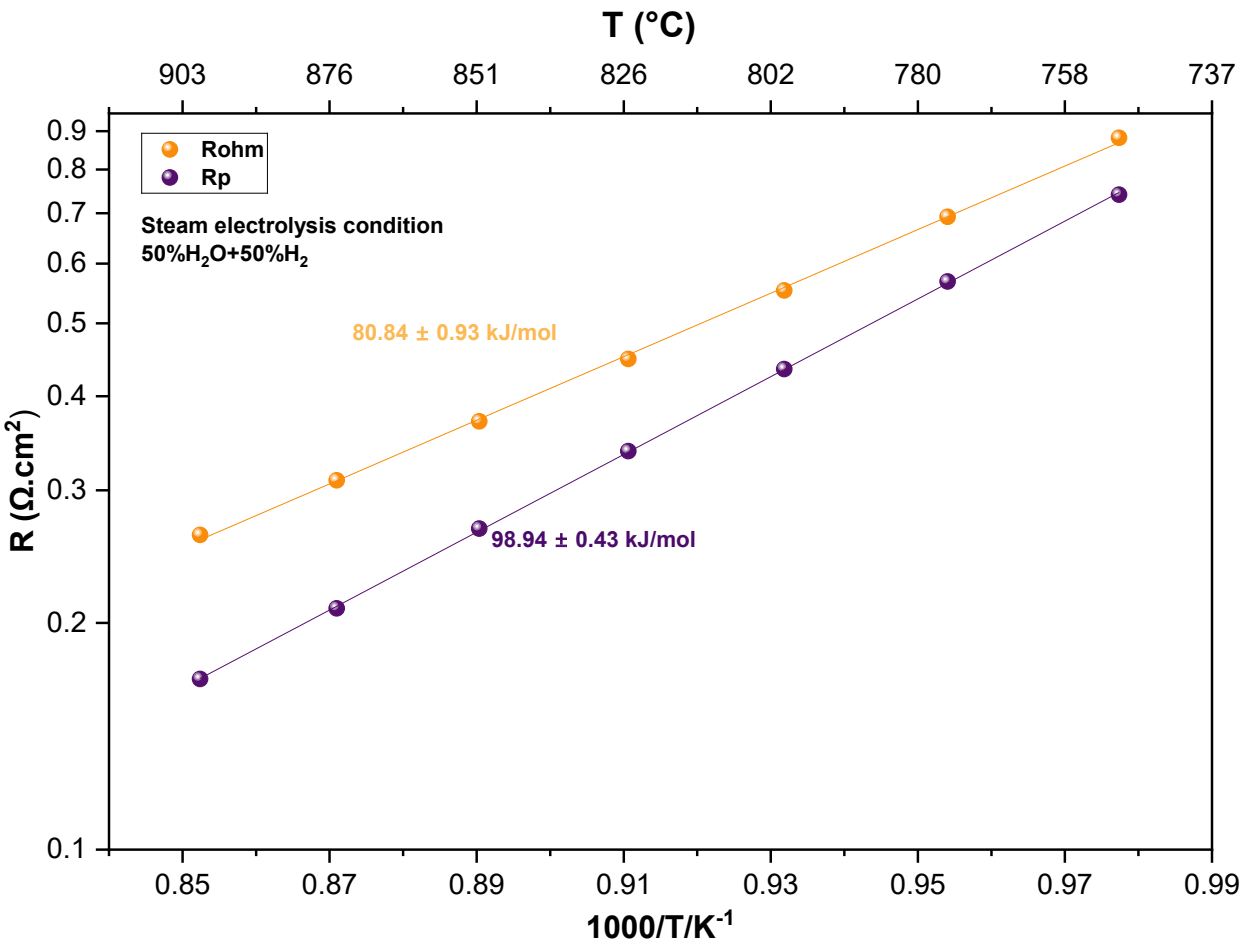


Figure 16: Derived activation energy for the Ohmic and polarization resistances in steam electrolysis conditions

### 3.2.3. Distribution of relaxation times (DRT)

The EIS data visualized as a Nyquist plot in Fig 17 were analyzed by distribution of relaxation times (DRT) to separate overlapping physicochemical processes. A regularization parameter $\lambda = 10^{-5}$ was used because it produced stable reconstructions with a constant sum of square residuals (SSR) compared to the experimental impedance. Figure 18 shows the DRT spectra for the selected 19 µm PDC10 symmetrical cell. Four clear peaks are present across the measured temperature range. Based on the resolved time constants in our symmetrical cell configuration, we categorize the process as follows: high-frequency peak $P_1$ (>100Hz), mid-frequency peaks $P_{2a}$ and $P_{2b}$ (1-100Hz), and a dominant low-frequency peak $P_3$ (0.1-1Hz), which is the rate-determining step. All peaks increase in area as temperature decreases, indicating that each is thermally activated.

To quantify each contribution and extract resistance associated with individual processes for Arrhenius analysis, the impedance spectra were next fitted with an equivalent circuit model (ECM).

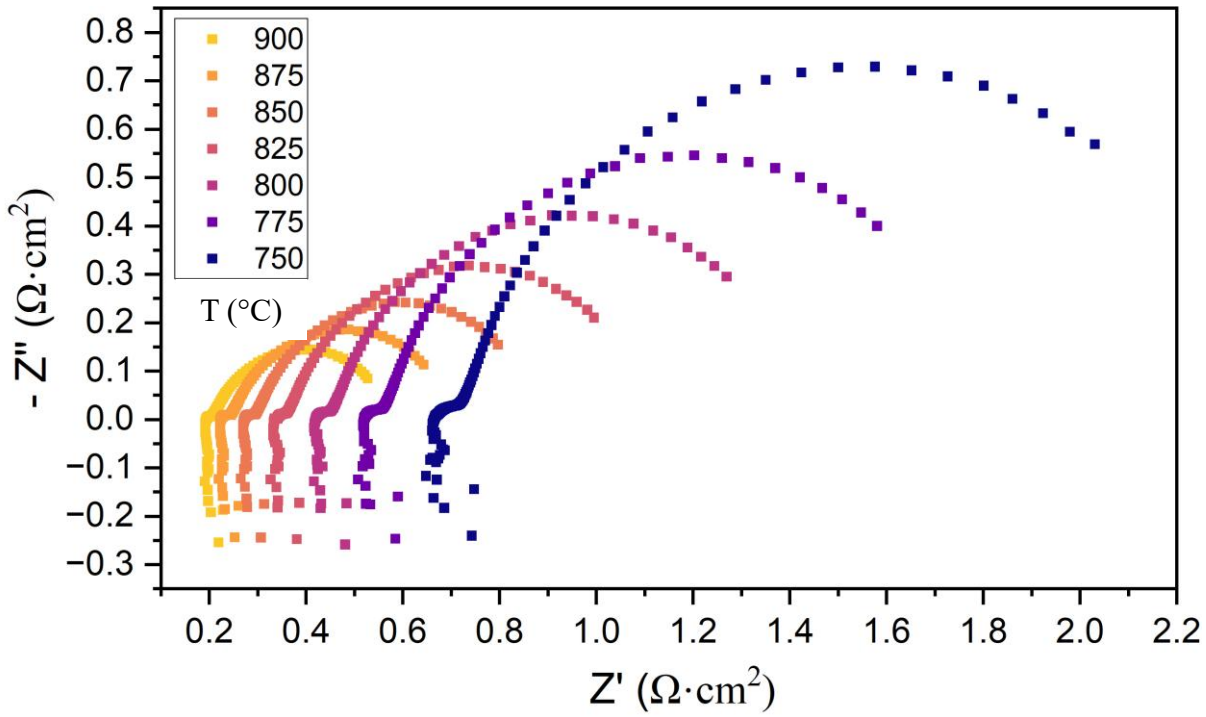


Figure 17: Nyquist plot for the 19 µm symmetrical PDC10, under temperature variation during steam electrolysis conditions

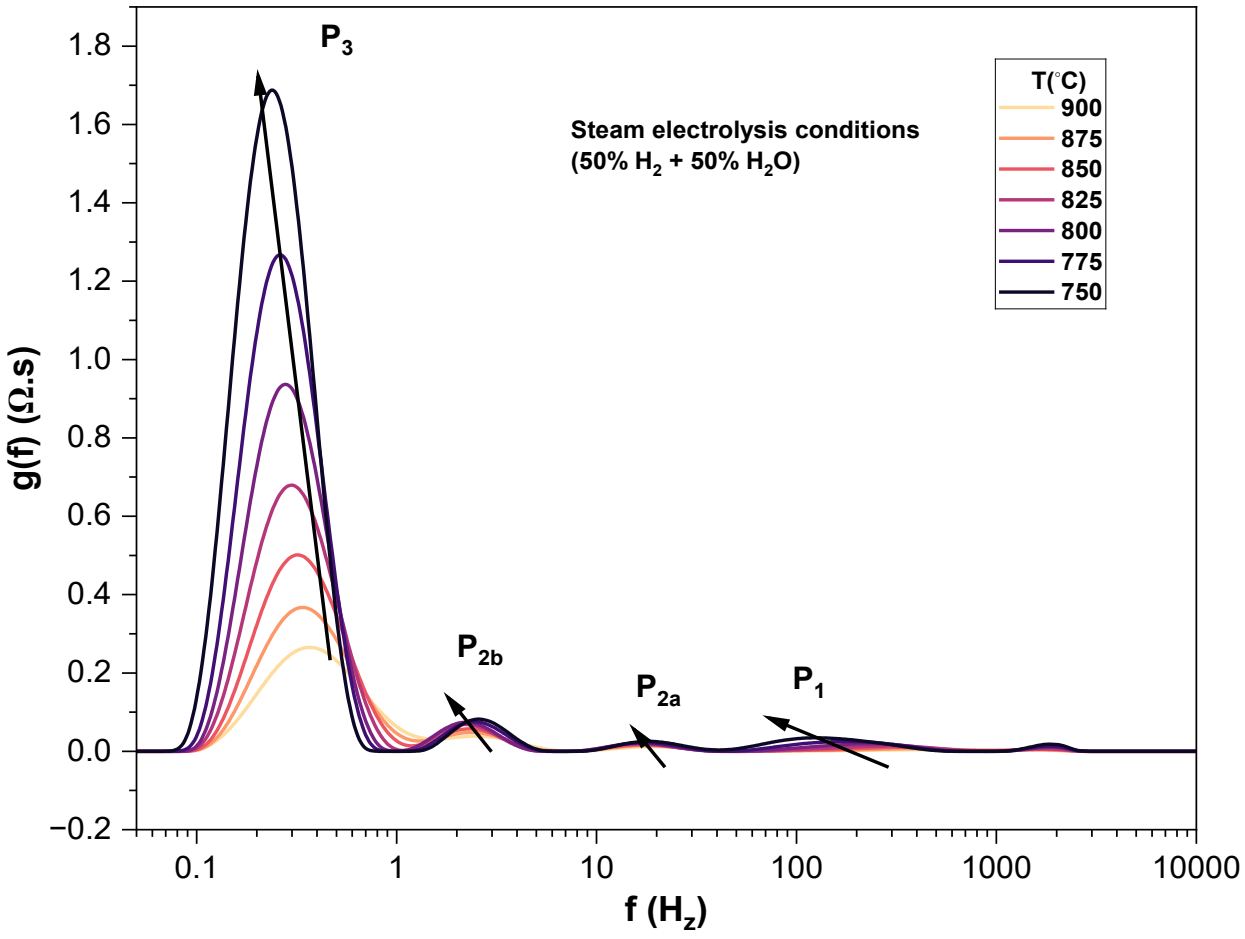


Figure 18: DRT of the Nyquist plot for the 19 µm symmetrical PDC10, under temperature variation during steam electrolysis conditions, with the arrow indicating the different peak.

### 3.2.4. ECM development

After the DRT analysis, several equivalent circuit models (ECMs) were tested using complex nonlinear least squares (CNLS) fitting to reproduce the experimental impedance spectra and to extract physically meaningful resistances and time constants. Initial attempts using a series model of an inductance, an ohmic resistance with three RQ branches (I-$R_\Omega$-3RQ) did not produce acceptable fits, the residuals were not randomly distributed, and the extracted resistances showed no consistent temperature trend, indicating an inadequate model structure.

Guided by the DRT peaks, the impedance spectra were next fitted with an ECM consisting of 2RQ plus a Gerischer element (Figure 19) in series with the ohmic resistance and an inductance to capture high-frequency wiring effects (I-$R_\Omega$-$RQ_1$-G-$RQ_2$). This model provides a good fit for the recorded Nyquist plot under steam electrolysis conditions at 900 °C (Figure 20).

The DRT of the fitted data was then simulated with the Relaxis® circuit simulator to evaluate the quality of the fit. The DRT overlapped closely with the fit at 900 °C (Figure 21), confirming that the circuit captures the main relaxation processes. Another simulation was made to see the contribution of the Gerischer element and the $RQ_2$. Comparing the DRT of the individual element with the DRT of the actual fit (Figure 22) shows that the Gerischer element maps onto the mid-frequency contribution, while the $RQ_2$ overlaps with the dominant low-frequency peak (0.1-1Hz). Knowing the complexity of the Gerischer element and the fact that it can exhibit several smaller peaks, it has been attributed to the mid-frequency peaks $P_{2a}$ and $P_{2b}$. This mapping supports the physical assignment that the process associated with $RQ_2$ might be the rate-determining step under these conditions.

The quality of fit was quantified by residuals and Chi² ($\chi^2$) statistic. The residuals of the fit showed for both real and imaginary parts an absolute error of 1.2 mΩ (Figure 23), with the $\chi^2 = 7.3 \times 10^{-8}$.

The ohmic resistance and the resistances of the three processes were extracted from the fitted EIS in the temperature range of 900 °C to 750 °C and plotted as Arrhenius plots in Figure 24 and Figure 25. Arrhenius fits of each fitted resistance (using equation 11) yielded activation energies for the individual processes, which we use below to propose physical assignments and to compare with literature.

$$\boldsymbol{lnR = -ln\sigma_0 + \frac{E_a}{RT}} \tag{11}$$

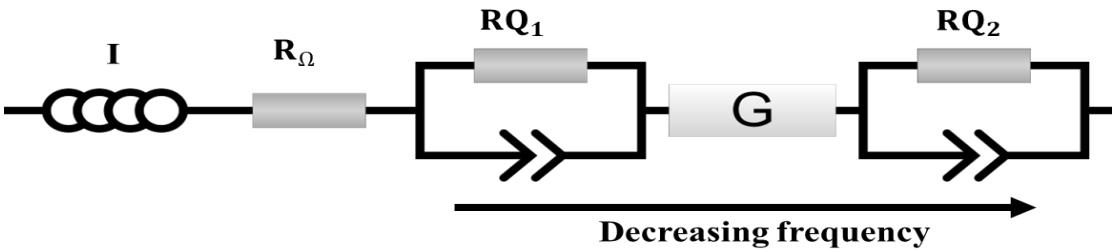


Figure 19: Proposed ECM for CNLS fit of the recorded Nyquist plot data.

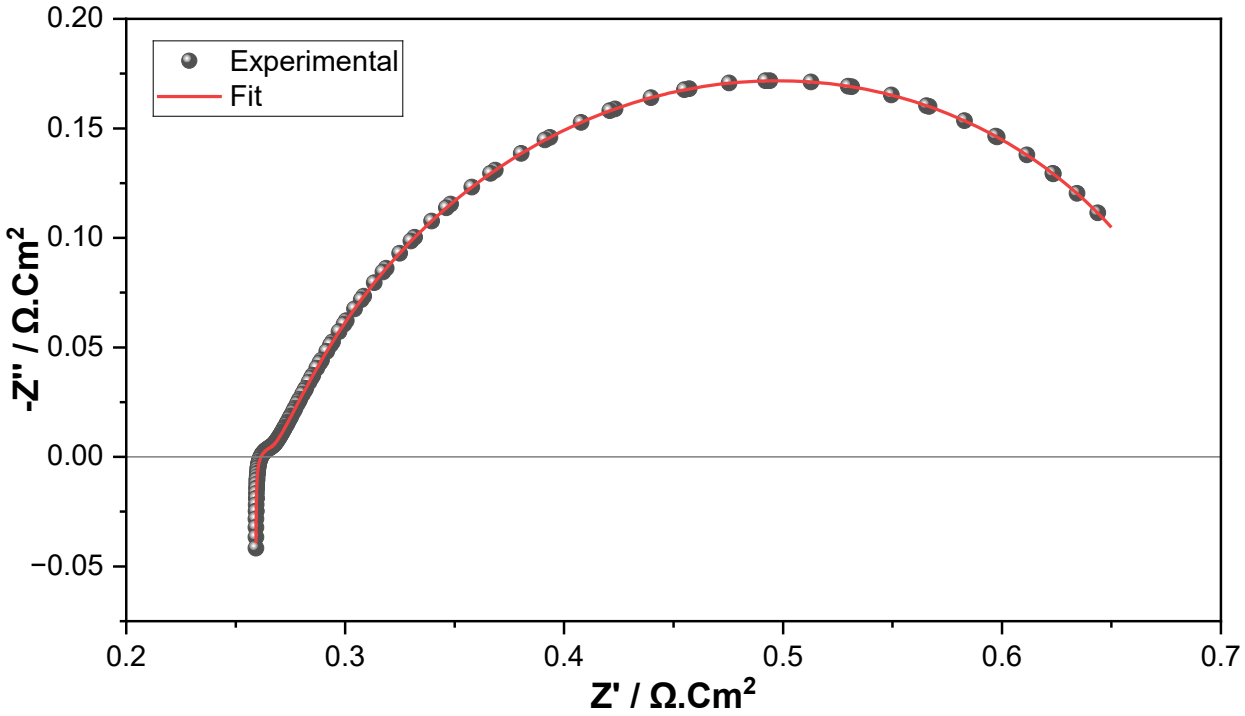


Figure 20: Nyquist plot from experimental data and the respective fit at 900 °C.

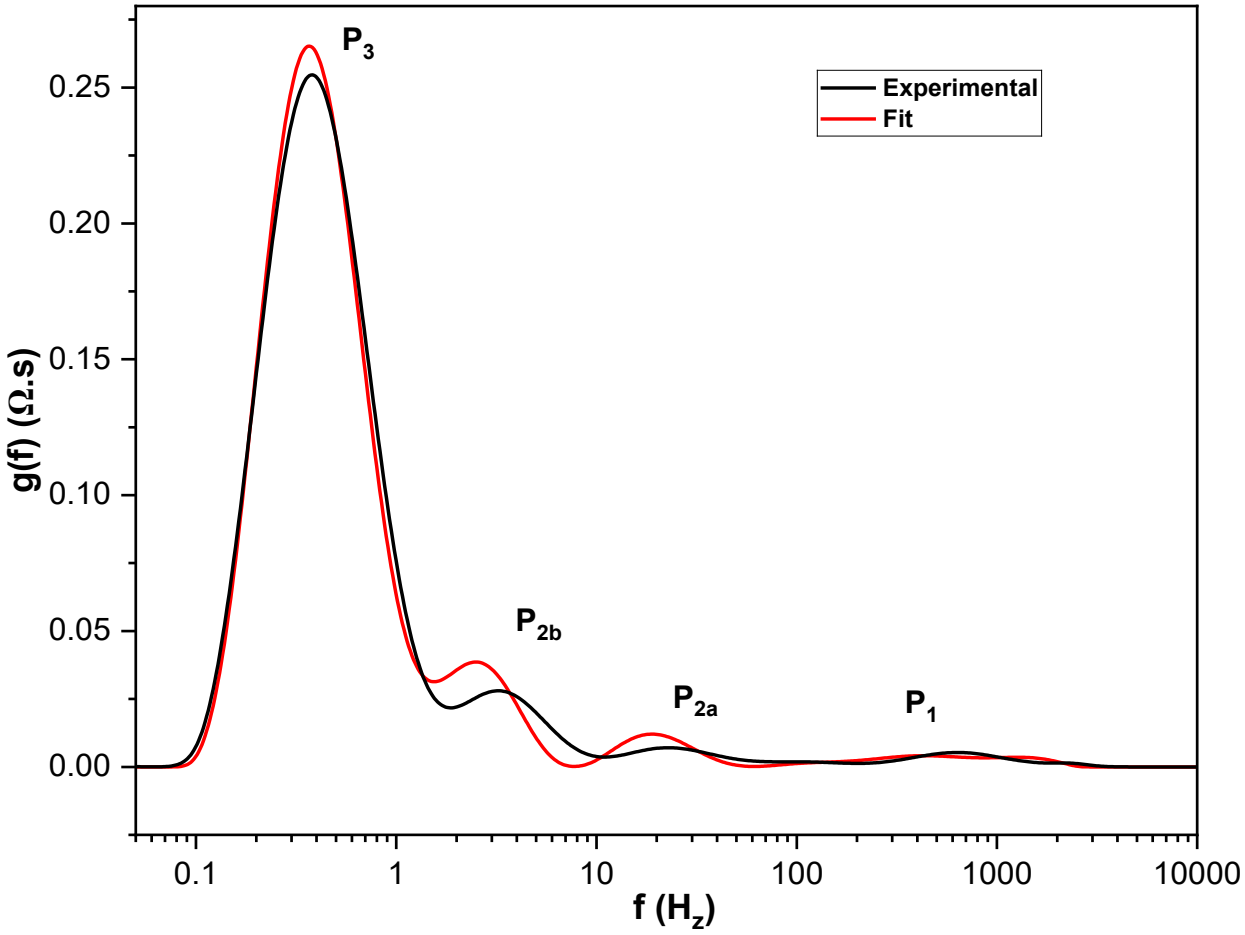


Figure 21: DRT from experimental data and the respective fit at 900 °C.

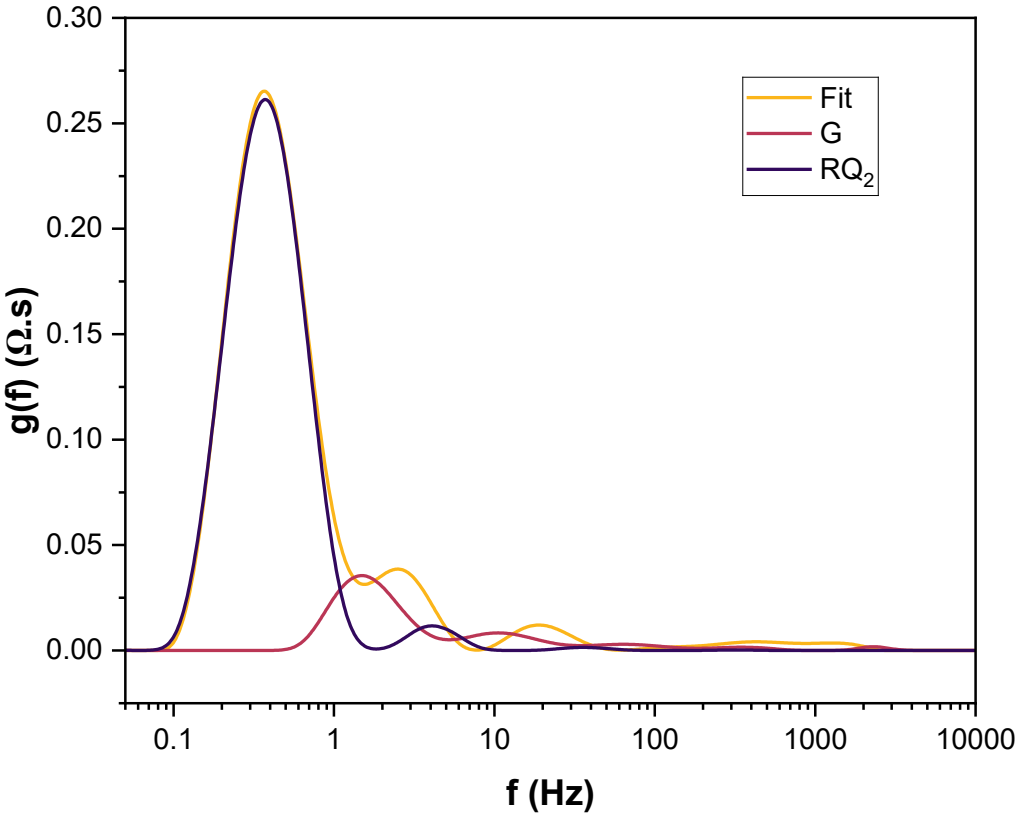


Figure 22: Decomposing DRT from the fit, the Gerischer, and the $RQ_2$ at 900 °C.

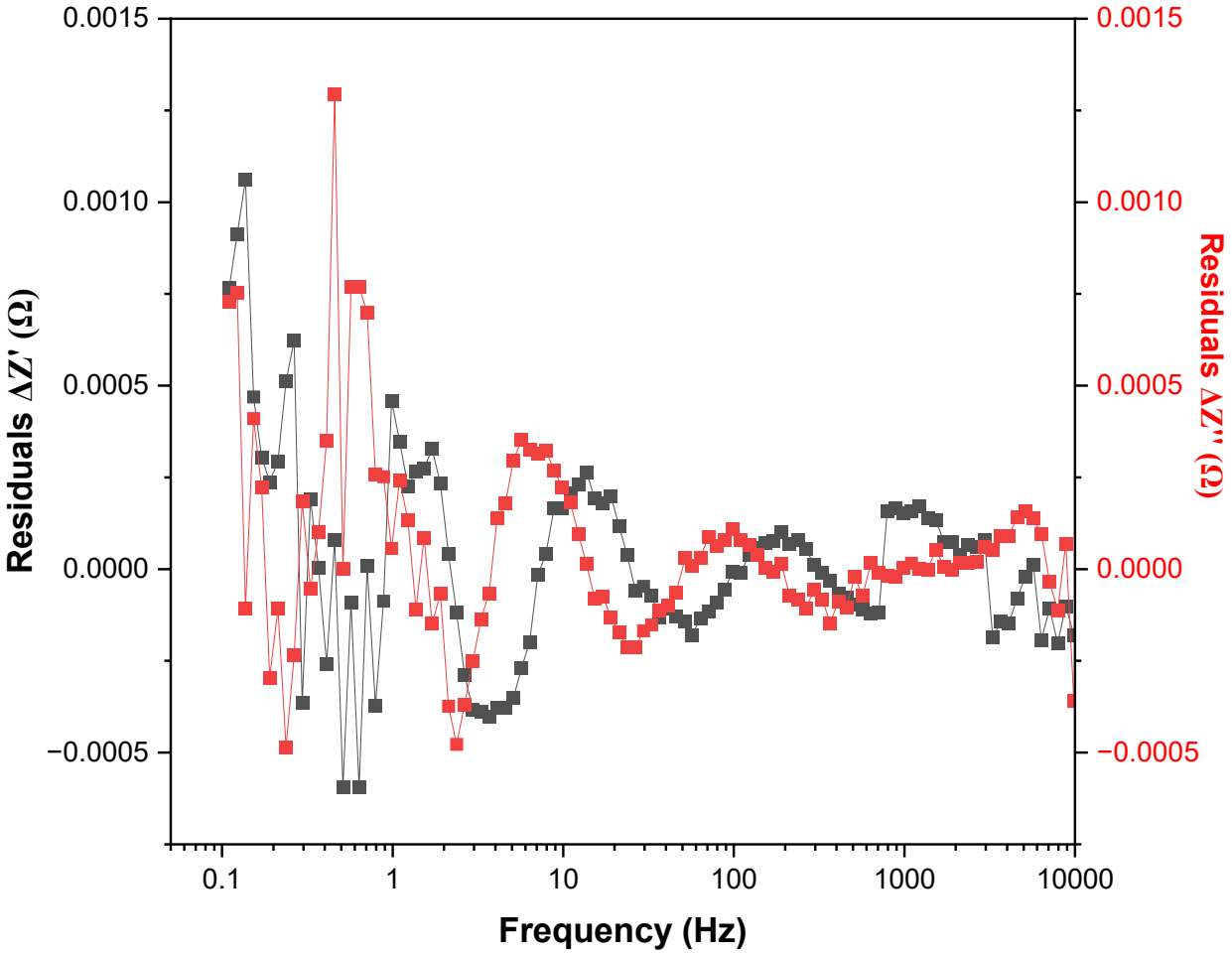


Figure 23: Residuals of the fit at 900 °C.

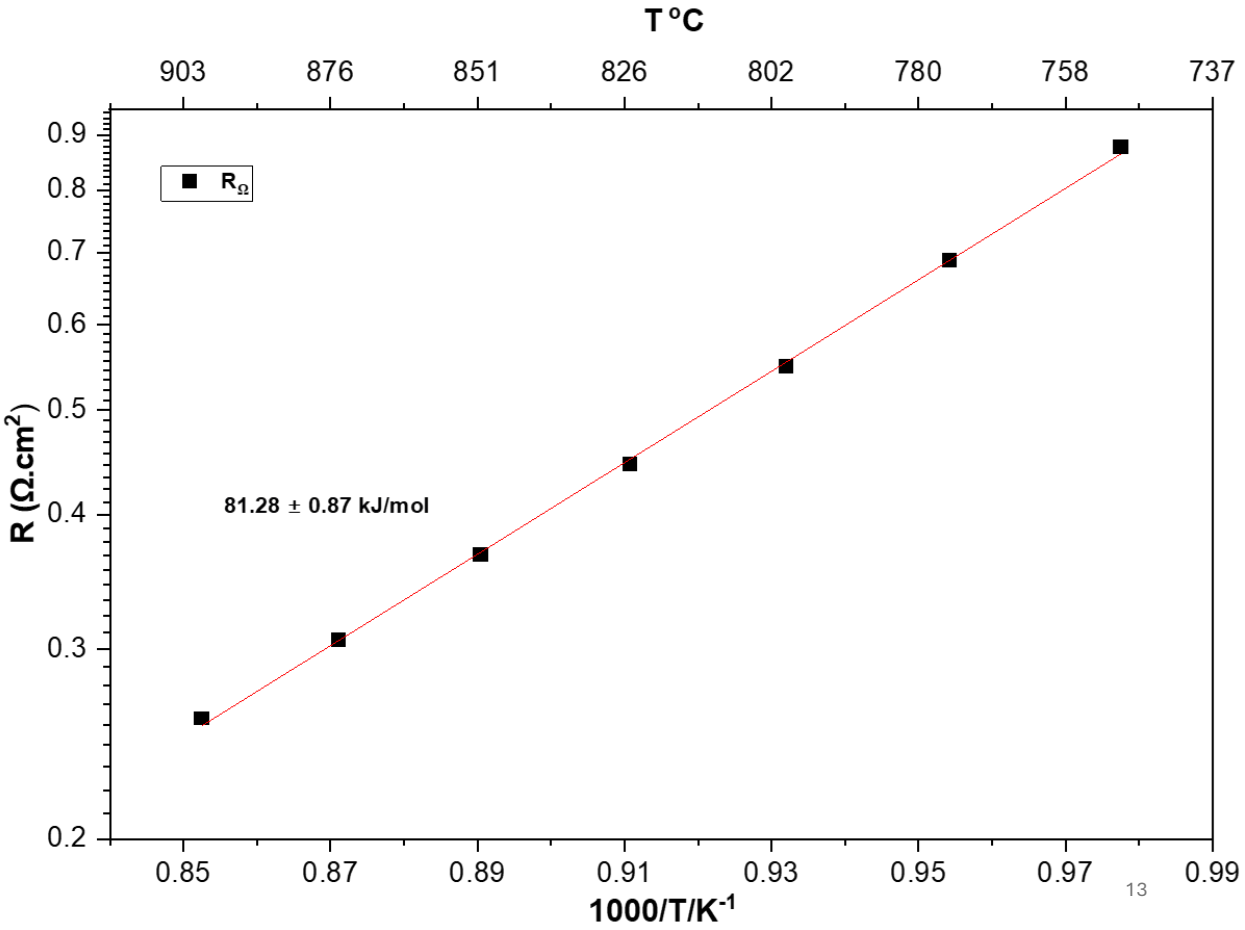


Figure 24: Arrhenius plot of the ohmic resistance from the fit in steam electrolysis conditions.

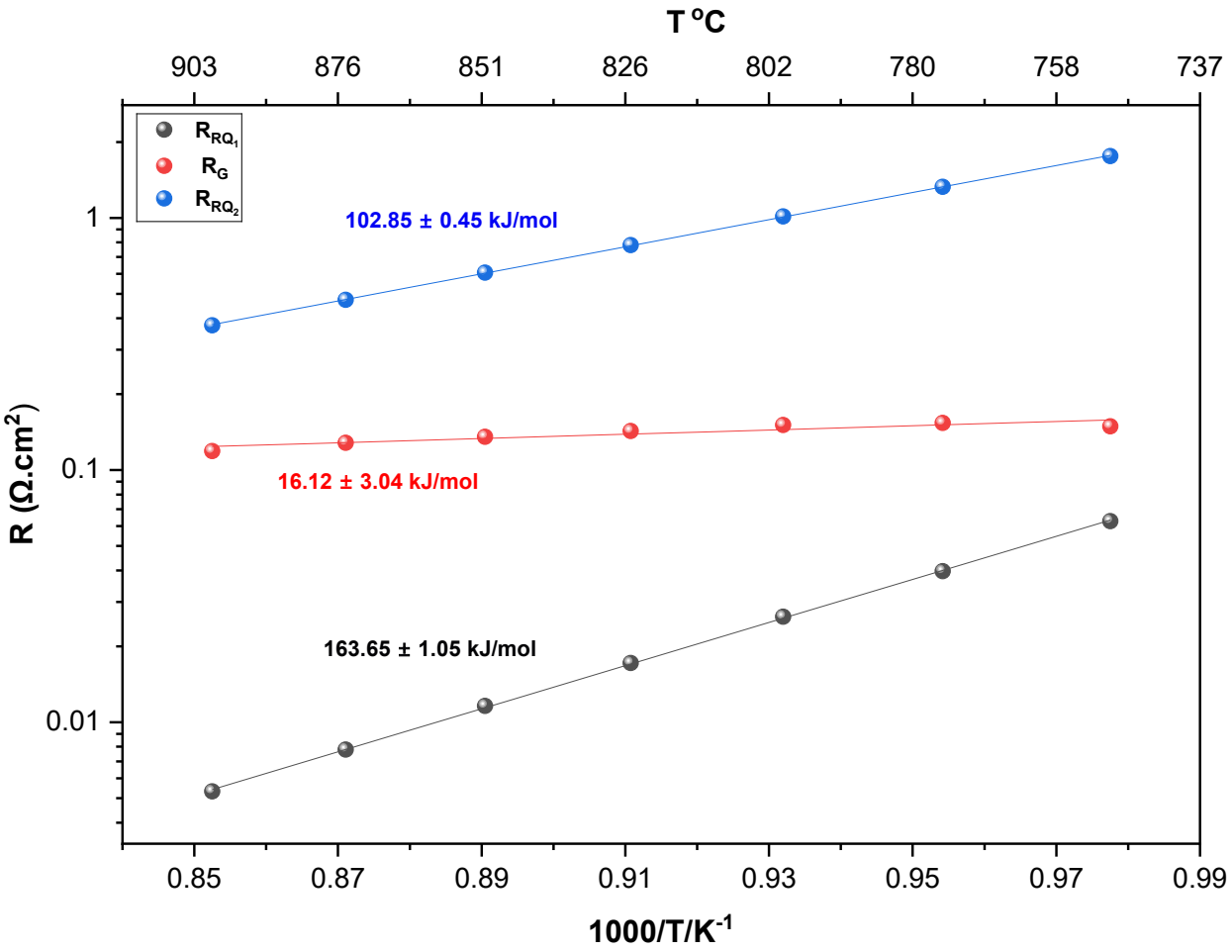


Figure 25: Arrhenius plot of the resistances $R_{RQ_1}$, $R_G$, $R_{RQ_2}$ from the fit.

### 3.2.5. Evaluation of the activation energies

To gain further insight into the physical origin of the electrochemical processes resolved by DRT and ECM fitting, activation energies were extracted to provide a useful meaning of each relaxation feature.

As expected for an electrolyte-supported cell, the thick 250 µm 8YSZ electrolyte is the main contributor to the ohmic resistance ($R_\Omega$) as part of his activation energy 81.28 kJ. $mol^{-1}$ which is close to the reported 88 kJ. $mol^{-1}$ in the literature for the YSZ electrolyte [66].

An apparent activation energy of 102.85 kJ. $mol^{-1}$ for resistance $R_{RQ_2}$ was measured for the dominant low-frequency process. This value is close to literature reports for the charge transfer on the ceria surface in the Ni-GDC symmetrical cell (112 kJ. $mol^{-1}$ ) [67]. The $R_{RQ_1}$ process shows a higher activation energy, 163.65 kJ. $mol^{-1}$, and appears at a frequency (>100Hz). Such a high activation energy is usually attributed to a charge transfer process in the electrodes [68], [69].

The fitted Gerischer element displays a very low apparent activation energy (16.12 $\mathrm{kJ.mol^{-1}}$) in our PDC10 symmetrical cell. In other SOFC/SOEC studies, the Gerischer response is often associated with surface kinetics coupled with $O^{2-}$ diffusion and has been reported with much higher activation energies, 140 $\mathrm{kJ.mol^{-1}}$ [70], [71]. Further tests are therefore required to clarify the physical origin of the Gerischer.

### 3.2.6. Effect of gas partial pressure

To examine the different processes at the fuel electrode, the $H_2$ composition was varied.

For the 19 µm cell, EIS data records at 850 °C while keeping the $H_2O$ constant and varying the $H_2$ and the $N_2$ are presented as a Nyquist plot in Figure 26. The Nyquist plot shows that the total polarization resistance increases as $p(H_2)$ decreases. EIS data were then fitted using the ECM guided by DRT (I-$R_\Omega$-$RQ_1$-G-$RQ_2$).

When the fitted resistances are plotted versus $p(H_2)$ (Figure 28), $R_{RQ_2}$ shows a clear dependence on hydrogen concentration. $R_{RQ_2}$ decreases as $p(H_2)$ increases, consistent with the observed overall Rp change in the Nyquist plots. In contrast, both $R_{RQ_1}$, $R_G$ show negligible dependence on $p(H_2)$. Correspondingly, the DRT spectra (Figure 27) confirm that peaks $P_1$, $P_{2a}$ and $P_{2b}$ are essentially insensitive to hydrogen content, while the dominant low-frequency peak P3 tracks $p(H_2)$ strongly.

The strong $H_2$ sensitivity and apparent rate order $p(H_2)^{-0.43}$ of $R_{RQ_2}$, appears to be close to 0.5, indicating that the process $P_3$ represents the adsorption and dissociation of the hydrogen on the ceria surface [72]. This confirms our hypothesis that the $R_{RQ_2}$ is associated with a hydrogen-related charge transfer and is the rate-determining step. The Gerischer term and the $R_{RQ_1}$ branch being $H_2$-Insensitive are interpreted as processes governed by solid-state or interfacial transport that do not depend on gas-phase hydrogen under these conditions. More experiments are then required to explain all the processes happening in the symmetrical PDC10.

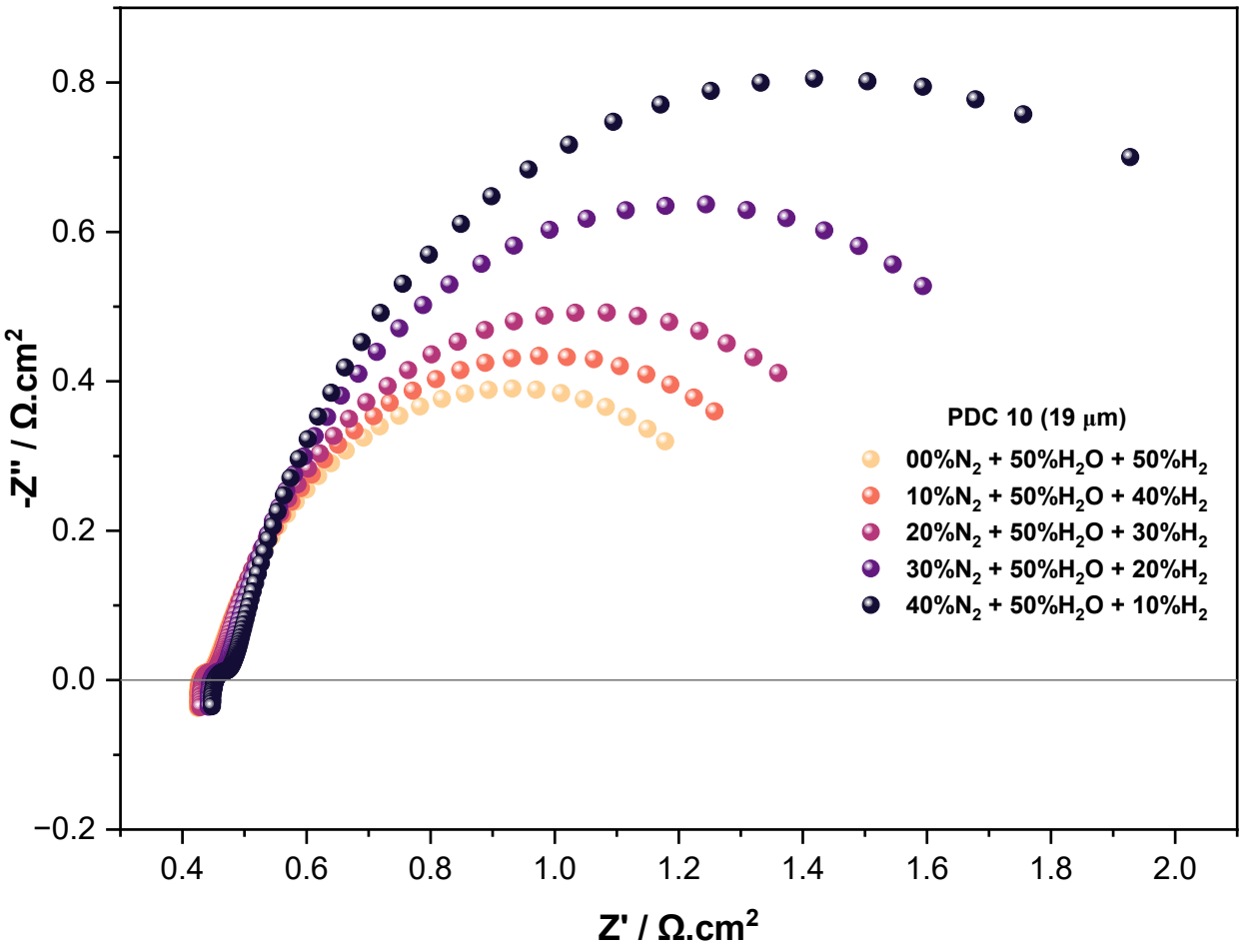


Figure 26: Nyquist plot of symmetrical PDC10 (19 µm) under gas variation at 850 °C.

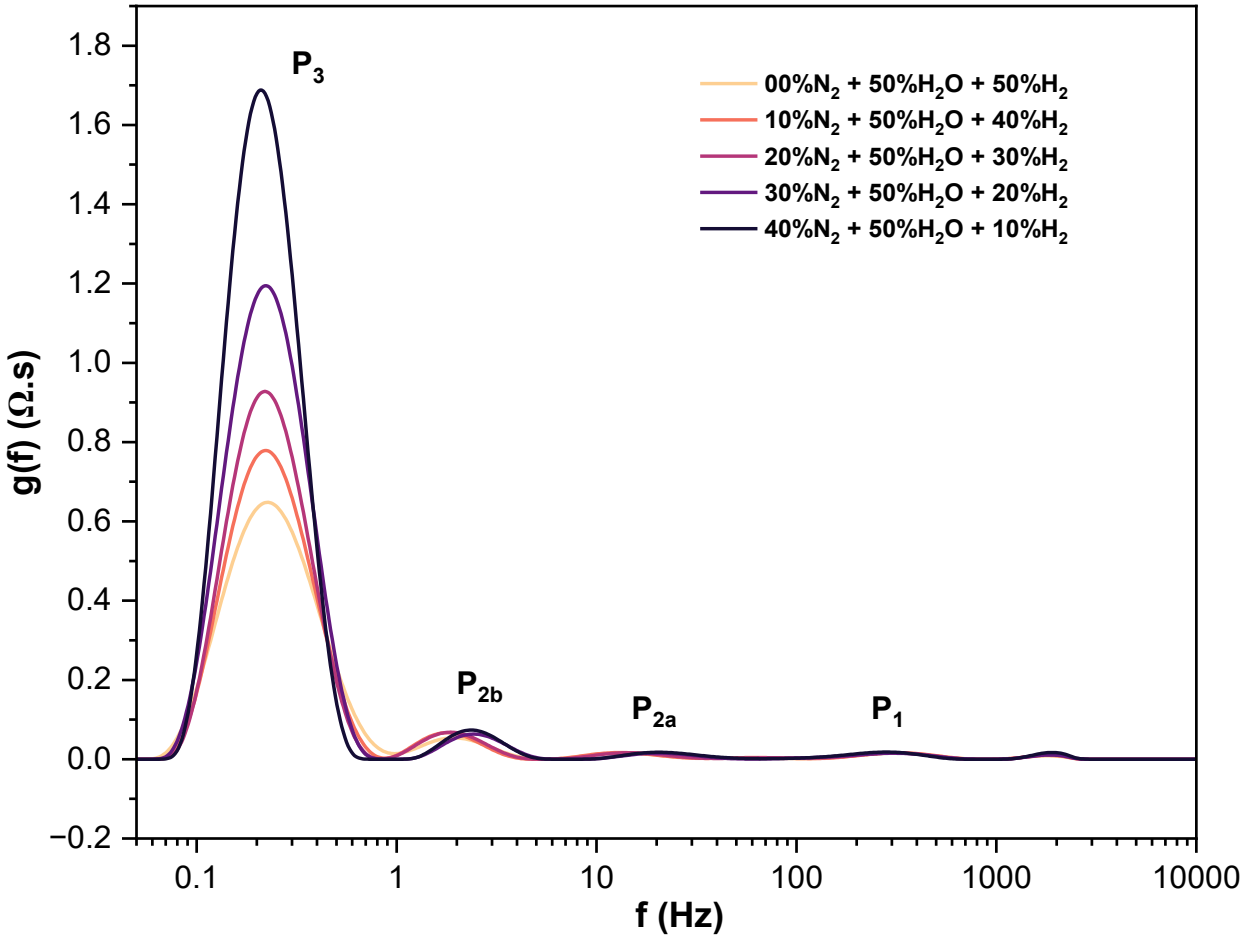


Figure 27: DRT of the Nyquist plot for the 19 µm symmetrical PDC10, under gas variation at 850 °C.

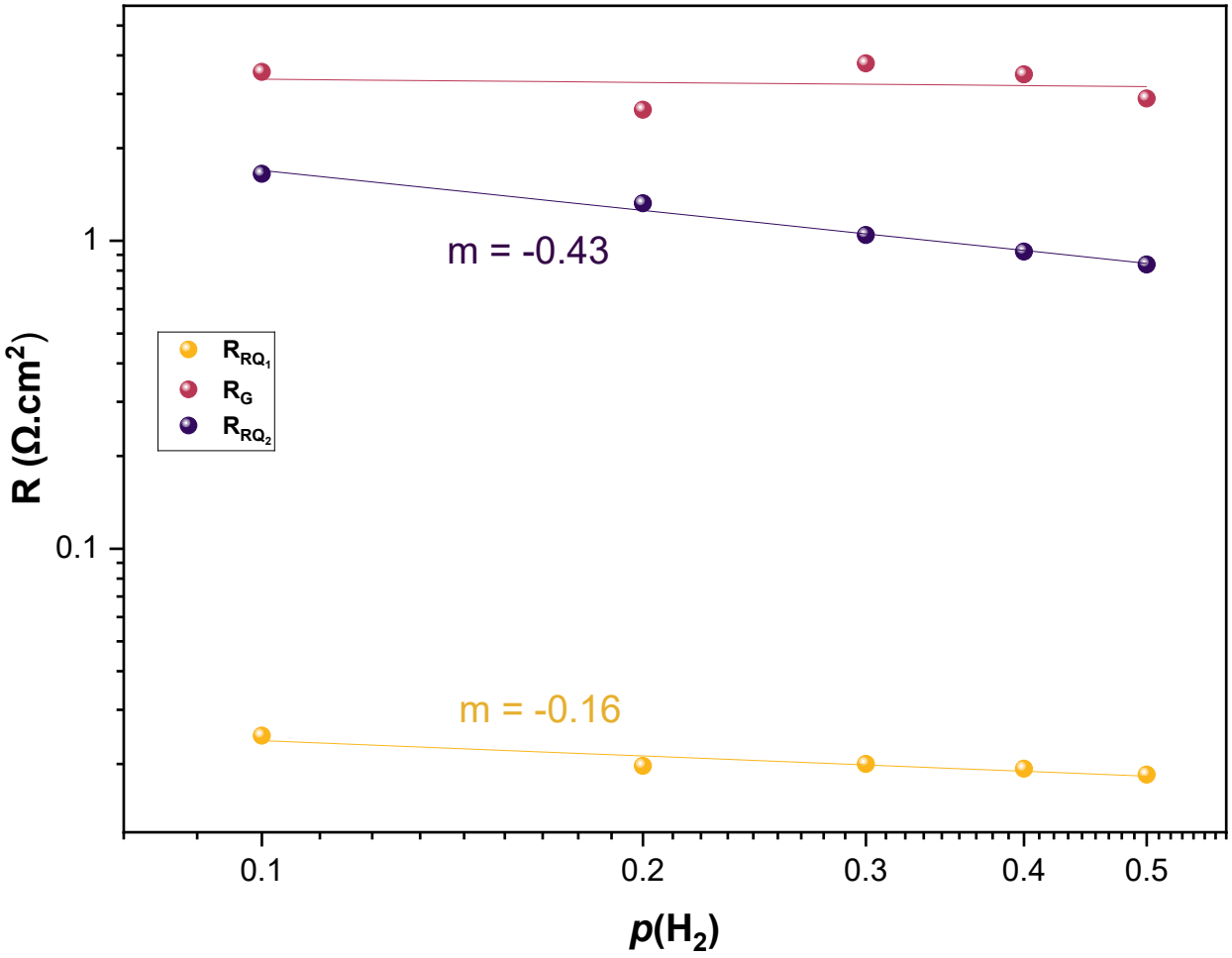


Figure 28: Dependency of the resistances $R_{RQ_1}$, $R_G$, $R_{RQ_2}$ with respect to $H_2$

**Conclusion**

This chapter presents a comprehensive investigation into the performance of our symmetrical PDC10. SEM showed that both cells look well-connected, but the thinner (19 µm ) layer gave better electrochemical performance and was chosen for detailed study. EIS + DRT decomposed the response into three main processes: a dominant low-frequency branch ($RQ_2$), a mid-frequency Gerischer contribution, and a high-frequency branch ($RQ_1$). Varying $p(H_2)$ revealed that only the low-frequency resistance is hydrogen-sensitive, identifying it as a hydrogen-related charge-transfer/adsorption step that limits kinetics under our conditions; the Gerischer and $RQ_1$ processes are essentially gas-insensitive and likely reflect short-range solid-state or lattice/redox phenomena.

# GENERAL CONCLUSION AND PERSPECTIVES

## GENERAL CONCLUSION AND PERSPECTIVES

This study investigated the electrochemical characterization of symmetrical PDC10 ($Pr_{0.1}Ce_{0.9}O_{2-\delta}$) electrodes using two cells with a nominal PDC10 layer thickness of 46 µm and 19 µm. The thinner 19 µm electrode was selected for detailed study because it exhibited better performance in steam electrolysis at 850 °C.

The temperature dependence of the total polarization resistance did not reveal a single consistent trend for all gas compositions, indicating overlapping and temperature-dependent contributions from several processes. Therefore, DRT analysis and ECM fitting were used to decompose the impedance into individual processes. For the 19 µm cell, three main contributions were identified (2RQ and a Gersicher element).

Arrhenius analysis of the fitted resistances gave apparent activation energies of 163.65 $kJ.mol^{-1}$ ($R_{RQ_1}$), 102.85 $kJ.mol^{-1}$ ($R_{RQ_2}$), and 16.12 $kJ.mol^{-1}$($R_G$). Combining frequency, gas-pressure dependence, and $E_a$ values led to the following working assignments:

- process $P_3$ is strongly hydrogen sensitive and shows an apparent reaction order near 0.5, consistent with a hydrogen-related surface process;
- process $P_1$ characterized by a large activation energy and weak hydrogen dependence, is attributed to an intrinsic electrode charge-transfer step;
- process $P_{2a}, P_{2b}$ with low apparent activation energy and unclear gas dependence, remains unresolved in its physical origin based on the present data.

The gas-partial-pressure study confirmed that the dominant low-frequency process ($RQ_2$) is hydrogen-sensitive and likely controls the electrode kinetics in our PDC10 symmetric cells. The Gerischer contribution and the precise nature of the high-energy $RQ_1$ process remain ambiguous and require targeted follow-up investigations.

In summary, PDC10 electrodes demonstrate promising behavior as Ni-free fuel electrodes: the dominant limitation under our conditions is a hydrogen-controlled surface charge-transfer step that is identifiable by EIS+DRT+ECM. The decomposition and kinetic fingerprints obtained in this study provide a robust foundation for future experiments and microstructural optimizations aimed at enhancing the activity and the durability of PDC-based electrodes for high-temperature hydrogen/syngas production.

Improvement of the equivalent circuit model is further required to better resolve and understand the mid-frequency processes. Future work could also explore the use of PDC symmetrical cells for power generation and evaluate their potential as bifunctional catalysts for reversible SOC applications.

## REFERENCES

[1] "COP27 Reaches Breakthrough Agreement on New 'Loss and Damage' Fund for Vulnerable Countries _ UNFCCC".

[2] G. Schiller et al., "Solar heat integrated solid oxide steam electrolysis for highly efficient hydrogen production," J Power Sources, vol. 416, pp. 72–78, Mar. 2019, doi: 10.1016/j.jpowsour.2019.01.059.

[3] M. Carmo, D. L. Fritz, J. Mergel, and D. Stolten, "A comprehensive review on PEM water electrolysis," Apr. 22, 2013. doi: 10.1016/j.ijhydene.2013.01.151.

[4] R. Küngas, " Review—Electrochemical CO 2 Reduction for CO Production: Comparison of Low- and High-Temperature Electrolysis Technologies ," J Electrochem Soc, vol. 167, no. 4, p. 044508, Jan. 2020, doi: 10.1149/1945-7111/ab7099.

[5] H. Ito, T. Maeda, A. Nakano, and H. Takenaka, "Properties of Nafion membranes under PEM water electrolysis conditions," Aug. 2011. doi: 10.1016/j.ijhydene.2011.05.127.

[6] J. Brauns and T. Turek, "Alkaline water electrolysis powered by renewable energy: A review," Feb. 01, 2020, MDPI AG. doi: 10.3390/pr8020248.

[7] S. Shiva Kumar and V. Himabindu, "Hydrogen production by PEM water electrolysis – A review," Dec. 01, 2019, KeAi Communications Co. doi: 10.1016/j.mset.2019.03.002.

[8] H. Zheng, Y. Tian, L. Zhang, B. Chi, J. Pu, and L. Jian, "La0.8Sr0.2Co0.8Ni0.2O3-Δ impregnated oxygen electrode for H2O/CO2 co-electrolysis in solid oxide electrolysis cells," J Power Sources, vol. 383, pp. 93–101, Apr. 2018, doi: 10.1016/j.jpowsour.2018.02.041.

[9] A. Hauch et al., "Recent advances in solid oxide cell technology for electrolysis," Science (1979), vol. 370, no. 6513, Oct. 2020, doi: 10.1126/science.aba6118.

[10] P. Moçoteguy and A. Brisse, "A review and comprehensive analysis of degradation mechanisms of solid oxide electrolysis cells," Dec. 13, 2013. doi: 10.1016/j.ijhydene.2013.09.045.

[11] J. B. Hansen, "Solid oxide electrolysis - a key enabling technology for sustainable energy scenarios," Faraday Discuss, vol. 182, pp. 9–48, 2015, doi: 10.1039/c5fd90071a.

[12] X. Sun et al., "Durability of Solid Oxide Electrolysis Cells for Syngas Production," J Electrochem Soc, vol. 160, no. 9, pp. F1074–F1080, 2013, doi: 10.1149/2.106309jes.

[13] W. C. Chueh, Y. Hao, W. Jung, and S. M. Haile, “High electrochemical activity of the oxide phase in model ceria-Pt and ceria-Ni composite anodes,” Nat Mater, vol. 11, no. 2, pp. 155–161, 2012, doi: 10.1038/nmat3184.

[14] W. C. Chueh and S. M. Haile, “Electrochemistry of mixed oxygen ion and electron conducting electrodes in solid electrolyte cells,” Jul. 2012. doi: 10.1146/annurev-chembioeng-073009-101000.

[15] I. D. Unachukwu, V. Vibhu, I. C. Vinke, R. A. Eichel, and L. G. J. (Bert) de Haart, “Electrochemical and degradation behaviour of single cells comprising Ni-GDC fuel electrode under high temperature steam- and co-electrolysis conditions,” J Power Sources, vol. 556, Feb. 2023, doi: 10.1016/j.jpowsour.2022.232436.

[16] Y. Ji, J. Liu, T. He, J. Wang, and W. Su, “The effect of Pr co-dopant on the performance of solid oxide fuel cells with Sm-doped ceria electrolyte,” J Alloys Compd, vol. 389, no. 1–2, pp. 317–322, Mar. 2005, doi: 10.1016/j.jallcom.2004.08.018.

[17] Jonathan M. Witt, “Co-Electrolysis of Water and Carbon Dioxide by Gadolinia Doped Ceria Using Electrochemical Perturbations and Differential Frequency Resolved Mass Spectrometry,” University of Washington, Washington, 2021.

[18] R. Kumar, “Electrochemical Characterisation of Doped Ceria-based Materials as Fuel Electrode in Solid Oxide Cell Institute of Materials Science,” Forschungszentrum Jülich, Jülich, 2023.

[19] R. Bove and S. Ubertini, Eds., Modeling Solid Oxide Fuel Cells. Dordrecht: Springer Netherlands, 2008. doi: 10.1007/978-1-4020-6995-6.

[20] Y. Liu, L. Zuo, C. Jiang, D. Zheng, and B. Wang, “Composite electrolyte used for low temperature SOFCs to work at 390°C,” iScience, vol. 26, no. 7, Jul. 2023, doi: 10.1016/j.isci.2023.107002.

[21] J. Zhang, C. Lenser, N. H. Menzler, and O. Guillon, “Comparison of solid oxide fuel cell (SOFC) electrolyte materials for operation at 500 °C,” Solid State Ion, vol. 344, Jan. 2020, doi: 10.1016/j.ssi.2019.115138.

[22] V. N. Nguyen and L. Blum, “Syngas and synfuels from H2O and CO2: Current status,” Apr. 01, 2015, Wiley-VCH Verlag. doi: 10.1002/cite.201400090.

[23] M. A. Laguna-Bercero, “Recent advances in high temperature electrolysis using solid oxide fuel cells: A review,” Apr. 01, 2012. doi: 10.1016/j.jpowsour.2011.12.019.

[24] A. Buttler and H. Spliethoff, “Current status of water electrolysis for energy storage, grid balancing and sector coupling via power-to-gas and power-to-liquids: A review,” Feb. 01, 2018, Elsevier Ltd. doi: 10.1016/j.rser.2017.09.003.

[25] M. Reisert, A. Aphale, and P. Singh, “Solid oxide electrochemical systems: Material degradation processes and novel mitigation approaches,” Nov. 02, 2018, MDPI AG. doi: 10.3390/ma11112169.

[26] Bintou Issa DEMBELE, “SALT-WATER ELECTROLYSIS FOR GREEN HYDROGEN ECONOMY(2)(original),” WASCAL, 2023.

[27] L. Dittrich, “Tailoring of the Synthesis Gas Composition during High-Temperature Co-Electrolysis Tailoring der Synthesegas-Zusammensetzung während der Herstellung über Hochtemperatur-Ko-Elektrolyse.”

[28] Jeanmonod and Guillaume, “Effects of impurities and local behavior characterization using active thermography on solid oxide electrolysis cells,” Groupe SCI STI JVH, 2021.

[29] E. C. Shin, J. Ma, P. A. Ahn, H. H. Seo, D. T. Nguyen, and J. S. Lee, “Deconvolution of Four Transmission-Line-Model Impedances in Ni-YSZ/YSZ/LSM Solid Oxide Cells and Mechanistic Insights,” Electrochim Acta, vol. 188, pp. 240–253, Jan. 2016, doi: 10.1016/j.electacta.2015.11.118.

[30] Y. Tian et al., “High performance and stability of double perovskite-type oxide NdBa0.5Ca0.5Co1.5Fe0.5O5+δ as an oxygen electrode for reversible solid oxide electrochemical cell,” Journal of Energy Chemistry, vol. 43, pp. 108–115, Apr. 2020, doi: 10.1016/j.jechem.2019.08.010.

[31] I. Sreedhar, B. Agarwal, P. Goyal, and S. A. Singh, “Recent advances in material and performance aspects of solid oxide fuel cells,” Sep. 01, 2019, Elsevier B.V. doi: 10.1016/j.jelechem.2019.113315.

[32] C. Su, W. Wang, M. Liu, M. O. Tadé, and Z. Shao, “Progress and Prospects in Symmetrical Solid Oxide Fuel Cells with Two Identical Electrodes,” Adv Energy Mater, vol. 5, no. 14, Jul. 2015, doi: 10.1002/aenm.201500188.

[33] Y. Tian et al., “Progress and potential for symmetrical solid oxide electrolysis cells,” Feb. 02, 2022, Cell Press. doi: 10.1016/j.matt.2021.11.013.

[34] Y. Huang, J. M. Vohs, and R. J. Gorte, “Characterization of LSM-YSZ Composites Prepared by Impregnation Methods,” J Electrochem Soc, vol. 152, no. 7, p. A1347, 2005, doi: 10.1149/1.1926669.

[35] C. M. Chun, G. Bhargava, and T. A. Ramanarayanan, “Metal Dusting Corrosion of Nickel-Based Alloys,” J Electrochem Soc, vol. 154, no. 5, p. C231, 2007, doi: 10.1149/1.2710215.

[36] H. He and J. M. Hill, “Carbon deposition on Ni/YSZ composites exposed to humidified methane,” Appl Catal A Gen, vol. 317, no. 2, pp. 284–292, Feb. 2007, doi: 10.1016/j.apcata.2006.10.040.

[37] Y. Matsuzaki and I. Yasuda, “The poisoning effect of sulfur-containing impurity gas on a SOFC anode: Part I. Dependence on temperature, time, and impurity concentration,” 2000. [Online]. Available: www.elsevier.com/locate/ssi

[38] A. N. Busawon, D. Sarantaridis, and A. Atkinson, “Ni infiltration as a possible solution to the redox problem of SOFC anodes,” Electrochemical and Solid-State Letters, vol. 11, no. 10, 2008, doi: 10.1149/1.2959078.

[39] H. Kurokawa, T. Z. Sholklapper, C. P. Jacobson, L. C. De Jonghe, and S. J. Visco, “Ceria nanocoating for sulfur tolerant Ni-based anodes of solid oxide fuel cells,” Electrochemical and Solid-State Letters, vol. 10, no. 9, pp. 135–138, 2007, doi: 10.1149/1.2748630.

[40] H. Kim, C. Lu, W. L. Worrell, J. M. Vohs, and R. J. Gorte, “Cu-Ni Cermet Anodes for Direct Oxidation of Methane in Solid-Oxide Fuel Cells,” J Electrochem Soc, vol. 149, no. 3, p. A247, 2002, doi: 10.1149/1.1445170.

[41] E. Nikolla, J. Schwank, and S. Linic, “Direct Electrochemical Oxidation of Hydrocarbon Fuels on SOFCs: Improved Carbon Tolerance of Ni Alloy Anodes,” J Electrochem Soc, vol. 156, no. 11, p. B1312, 2009, doi: 10.1149/1.3208060.

[42] E. B. Watson and T. M. Harrison, “Zircon thermometer reveals minimum melting conditions on earliest earth,” Science (1979), vol. 308, no. 5723, pp. 841–844, May 2005, doi: 10.1126/science.1110873.

[43] J. Uecker, I. D. Unachukwu, V. Vibhu, I. C. Vinke, R. A. Eichel, and L. G. J. (Bert) de Haart, “Performance, electrochemical process analysis and degradation of gadolinium doped ceria as fuel electrode material for solid oxide electrolysis cells,” Electrochim Acta, vol. 452, Jun. 2023, doi: 10.1016/j.electacta.2023.142320.

[44] A. Nenning, M. Holzmann, J. Fleig, and A. K. Opitz, “Excellent kinetics of single-phase Gd-doped ceria fuel electrodes in solid oxide cells,” Mater Adv, vol. 2, no. 16, pp. 5422–5431, Aug. 2021, doi: 10.1039/d1ma00202c.

[45] Y. Zheng et al., “A review of high temperature co-electrolysis of H2O and CO2 to produce sustainable fuels using solid oxide electrolysis cells (SOECs): Advanced materials and technology,” Mar. 07, 2017, Royal Society of Chemistry. doi: 10.1039/c6cs00403b.

[46] E. Lay, G. Gauthier, and L. Dessemond, “Preliminary studies of the new Ce-doped La/Sr chromo-manganite series as potential SOFC anode or SOEC cathode materials,” Solid State Ion, vol. 189, no. 1, pp. 91–99, May 2011, doi: 10.1016/j.ssi.2011.02.004.

[47] C. Yang, A. Coffin, and F. Chen, “High temperature solid oxide electrolysis cell employing porous structured (La0.75Sr0.25)0.95MnO3 with enhanced oxygen electrode performance,” Int J Hydrogen Energy, vol. 35, no. 8, pp. 3221–3226, Apr. 2010, doi: 10.1016/j.ijhydene.2010.01.056.

[48] M. Á. Morales-Zapata, Á. Larrea, and M. Á. Laguna-Bercero, “Praseodymium and gadolinium doped ceria as oxygen electrode for solid oxide cell applications,” Boletín de la Sociedad Española de Cerámica y Vidrio, vol. 64, no. 2, pp. 138–149, Mar. 2025, doi: 10.1016/j.bsecv.2025.03.003.

[49] G. Accardo, G. Dell’Agli, L. Spiridigliozzi, S. P. Yoon, and D. Frattini, “On the oxygen vacancies optimization through Pr co-doping of ceria-based electrolytes for electrolyte-supported solid oxide fuel cells,” Int J Hydrogen Energy, vol. 45, no. 38, pp. 19707–19719, Jul. 2020, doi: 10.1016/j.ijhydene.2020.05.011.

[50] C. Ftikos, M. Nauer, and B. C. H. Steele, “Electrical Conductivity and Thermal Expansion of Ceria Doped with Pr, Nb and Sn,” 1993.

[51] M. V. Erpalov, A. P. Tarutin, N. A. Danilov, D. A. Osinkin, and D. A. Medvedev, “Chemistry and electrochemistry of $CeO_2$-based interlayers: Prolonging the lifetime of solid oxide fuel and electrolysis cells,” Russian Chemical Reviews, vol. 92, no. 10, p. RCR5097, Oct. 2023, doi: 10.59761/rcr5097.

[52] Gamry Instruments, “Basics of electrochemical impedance spectroscopy,” 734 Louis Drive, Warminster, PA 18974, USA, 2006. Accessed: Jun. 27, 2025. [Online]. Available: https://www.gamry.com/assets/Application-Notes/Basics-of-EIS.pdf

[53] A. E. Bumberger, A. Nenning, and J. Fleig, “Transmission line revisited - the impedance of mixed ionic and electronic conductors,” May 08, 2024, Royal Society of Chemistry. doi: 10.1039/d4cp00975d.

[54] C. P. Canales, Electrochemical Impedance Spectroscopy and Its Applications. 2021. doi: http://dx.doi.org/10.5772/intechopen.101636.

[55] A. Nechache, M. Cassir, and A. Ringuedé, “Solid oxide electrolysis cell analysis by means of electrochemical impedance spectroscopy: A review,” Jul. 15, 2014. doi: 10.1016/j.jpowsour.2014.01.110.

[56] T. G. Bergmann and N. Schlüter, “Introducing Alternative Algorithms for the Determination of the Distribution of Relaxation Times,” ChemPhysChem, vol. 23, no. 13, Jul. 2022, doi: 10.1002/cphc.202200012.

[57] N.-H. Communications and J. Weese, “Corr~puter Physics A reliable and fast method for the solution of Fredholm integral equations of the first kind based on Tikhonov regularization,” 1992.

[58] F. Kullmann, M. Mueller, A. Lindner, S. Dierickx, E. Mueller, and A. Weber, “DRT analysis and transmission line modeling of ceria based electrodes for solid oxide cells,” J Power Sources, vol. 587, Dec. 2023, doi: 10.1016/j.jpowsour.2023.233706.

[59] B. A. Boukamp, “Distribution (function) of relaxation times, successor to complex nonlinear least squares analysis of electrochemical impedance spectroscopy?,” Oct. 01, 2020, IOP Publishing Ltd. doi: 10.1088/2515-7655/aba9e0.

[60] A. Leonide, V. Sonn, A. Weber, and E. Ivers-Tiffée, “Evaluation and Modeling of the Cell Resistance in Anode-Supported Solid Oxide Fuel Cells,” J Electrochem Soc, vol. 155, no. 1, p. B36, 2008, doi: 10.1149/1.2801372.

[61] A. Kulikovsky and O. Shamardina, “A Model for PEM Fuel Cell Impedance: Oxygen Flow in the Channel Triggers Spatial and Frequency Oscillations of the Local Impedance,” J Electrochem Soc, vol. 162, no. 9, pp. F1068–F1077, 2015, doi: 10.1149/2.0911509jes.

[62] J. C. Ruiz-Morales, D. Marrero-López, J. Canales-Vázquez, and J. T. S. Irvine, “Symmetric and reversible solid oxide fuel cells,” Nov. 21, 2011. doi: 10.1039/c1ra00284h.

[63] D. M. Bastidas, S. Tao, and J. T. S. Irvine, “A symmetrical solid oxide fuel cell demonstrating redox stable perovskite electrodes,” J Mater Chem, vol. 16, no. 17, pp. 1603–1605, 2006, doi: 10.1039/b600532b.

[64] B. N. Park, “Electrochemical Properties of Ultrathin LiNi1/3Mn1/3Co1/3O2 (NMC111) Slurry-Cast Li-Ion Battery,” Crystals (Basel), vol. 14, no. 10, Oct. 2024, doi: 10.3390/cryst14100882.

[65] S. P. S. Badwal, “SOLID STATE IONICS Zirconia-based solid electrolytes: microstructure, stability and ionic conductivity,” 1992.

[66] C. Korte, A. Peters, J. Janek, D. Hesse, and N. Zakharov, “Ionic conductivity and activation energy for oxygen ion transport in superlattices-the semicoherent multilayer system YSZ (ZrO2 + 9.5 mol% Y2O3)/Y2O3,” Physical Chemistry Chemical Physics, vol. 10, no. 31, pp. 4623–4635, Jul. 2008, doi: 10.1039/b801675e.

[67] M. Riegraf, R. Costa, G. Schiller, K. A. Friedrich, S. Dierickx, and A. Weber, “Electrochemical Impedance Analysis of Symmetrical Ni/Gadolinium-Doped Ceria (CGO10) Electrodes in Electrolyte-Supported Solid Oxide Cells,” J Electrochem Soc, vol. 166, no. 13, pp. F865–F872, 2019, doi: 10.1149/2.0051913jes.

[68] P. Caliandro, A. Nakajo, S. Diethelm, and J. Van herle, “Model-assisted identification of solid oxide cell elementary processes by electrochemical impedance spectroscopy measurements,” J Power Sources, vol. 436, Oct. 2019, doi: 10.1016/j.jpowsour.2019.226838.

[69] D. Papurello, D. Menichini, and A. Lanzini, “Distributed relaxation times technique for the determination of fuel cell losses with an equivalent circuit model to identify physicochemical processes,” Electrochim Acta, vol. 258, pp. 98–109, Dec. 2017, doi: 10.1016/j.electacta.2017.10.052.

[70] C. Grosselindemann, N. Russner, S. Dierickx, F. Wankmüller, and A. Weber, “Deconvolution of Gas Diffusion Polarization in Ni/Gadolinium-Doped Ceria Fuel Electrodes,” J Electrochem Soc, vol. 168, no. 12, p. 124506, Dec. 2021, doi: 10.1149/1945-7111/ac3d02.

[71] A. Leonide, Y. Apel, and E. Ivers-Tiffee, “SOFC Modeling and Parameter Identification by Means of Impedance Spectroscopy,” ECS Trans, vol. 19, no. 20, pp. 81–109, Oct. 2009, doi: 10.1149/1.3247567.

[72] T. Zhu, H. E. Troiani, L. V. Mogni, M. Han, and S. A. Barnett, “Ni-Substituted Sr(Ti,Fe)O3 SOFC Anodes: Achieving High Performance via Metal Alloy Nanoparticle Exsolution,” Joule, vol. 2, no. 3, pp. 478–496, Mar. 2018, doi: 10.1016/j.joule.2018.02.006.